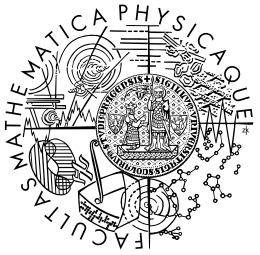

FACULTY
OF MATHEMATICS
AND PHYSICS
Charles University

HABILITATION THESIS

Nuclear magnetic resonance and density functional theory in solid state physics

Vojtěch Chlan

Prague 2020

I would like to thank to all my collaborators and colleagues as the presented results could hardly be accomplished without their contributions, samples, and discussions in the past years.
My greatest thanks belong to my wife and family for their support.

Contents

Introduction

Nuclear magnetic resonance (NMR) is a unique spectroscopic method for studying condensed matter: it gains information about the structure and important properties at atomic level, from the point of view of atomic nuclei. At the same time the measurement itself does not significantly perturb its point of interest, the electronic system. Namely, the resonant frequencies of nuclei are usually several orders of magnitude lower than analogous frequencies for electrons, phonons, or other species, which are thus affected by weak quasi-static fields only.

While NMR spectroscopy is a robust and irreplaceable method for studying structure and dynamics of liquids, where subtle electron-nuclear and inter-nuclear interactions can be captured in high-resolution spectra, the use of NMR in solid-state physics is much more limited. It is partly because of higher experimental demands in the solid-state NMR measurements, but to a great extent also due to the fact that analysis and interpretation of solid-state NMR spectra is more difficult. Ironically, the uniqueness of the method then becomes a curse: often there are no other experimental methods with adequate resolution to which the NMR results could be compared. The interpretation of NMR spectra of complex solids and magnetic materials may thus become extremely challenging.

The lack of other complementary experimental methods, fortunately, does not apply to methods for calculation of electronic structure. In this regard, the situation is in fact quite appropriate: the local character of NMR is exactly what supports such connection, since relatively small models in the electronic structure calculation are sufficient to describe the experimental spectra. Combination of the two methods, one experimental and one computational, but both focused on atomic scale, brings two main benefits:

- The calculations of spectroscopic parameters greatly simplify understanding of experimental NMR spectra, or even allow the interpretation in cases where it would be unfeasible otherwise.

- On the other hand, confronting the *ab initio* calculation with NMR experiment via the spectroscopic parameters supports the credibility of the calculated model. This applies not only to the properties being directly compared, but justifies the model as a whole, and thus also increases the reliability of other calculated physical properties – even those which cannot be obtained experimentally.

We have been applying and developing this comparative approach in the last decade. At the beginning we were concerned mostly with the local magnetic fields and gradients of electric fields in magnetically ordered materials, hence magnetic, multiferroic, and related materials were the subject of majority of the presented papers. More recently with advancement of computational possibilities our focus has been widened also to non-magnetic solids.

The thesis is structured in the following way: first chapter briefly introduces the nuclear magnetic resonance method, especially describes interactions of nuclear moments with local magnetic and electric fields – hyperfine magnetic field, electric field gradient, and chemical and Knight shift – and how they manifest in the NMR spectroscopy. Second chapter presents the methods of density functional

theory (DFT) calculations, which were used in our studies, with focus on local magnetic and electric fields: how the related quantities can be determined and how accurately, and also where the usual practice fails and other solutions need to be searched for. The way, how the approach of comparing NMR experiments and DFT calculations was applied in practice, is then presented in the last chapter in a form of commenting on the main results of the published papers.

1. Nuclear Magnetic Resonance in Solids

The nuclear magnetic resonance phenomenon is based on the interaction of nuclear moments with local magnetic and electric fields. The key prerequisite is the presence of nuclei with suitable nuclear spin I: nuclei with $I \geq \frac{1}{2}$ possess magnetic dipole moment and those with $I \geq 1$ possess electric quadrupole moment. The energy level of the ground state for such nuclei is then split by Zeeman interaction with magnetic field and/or by electric quadrupole interaction, and by exciting the transitions between the split levels it is possible to induce the NMR. The acquired NMR spectrum corresponds to the values of these local fields and thus carries essential spectroscopic information about the structure and other properties of the studied system.

The local magnetic and electric fields originate mostly by interaction of nucleus with electronic system, as is the case of magnetically ordered solids where the values of the local fields are directly reflected in the NMR spectrum. For non-magnetic solids the magnetic field is supplied as a very homogeneous static external magnetic field $\mathbf{B}_0$ and the resonance then probes subtle deviations from the value of $\mathbf{B}_0$. Regardless of the origin of the local fields, the key property of NMR (as for most spectroscopies) is the fact that, in general, nuclei in two different environments (e.g., nonequivalent crystal sites) have different values of the local fields, and therefore, different resonance frequencies in the NMR spectrum.

Besides the Coulomb interaction between the positive charge of the atomic nucleus and the surrounding electronic charge density, the nucleus interacts with electrons also via its nuclear moments: magnetic dipole moment and electric quadrupole moment. These interactions are usually termed the hyperfine interactions and are briefly described in the following paragraphs, accompanied by description of NMR shifts. Some of these quantities are, as well, of interest for Mössbauer spectroscopy, which was also utilized as an experimental method (together with or instead of NMR) in several of the presented works.

1.1 Hyperfine magnetic interaction

A nucleus with non-zero spin possesses nuclear dipole magnetic moment which can be – in analogy with electrons – expressed by units of nuclear magneton μ_N, a quantity about three orders of magnitude smaller than the Bohr magneton μ_B:

$$\mu_\mathrm{N} = \frac{e\hbar}{2m_p} \sim \frac{1}{1836}\mu_\mathrm{B}\,. \tag{1.1}$$

The interaction of nuclear spin with electrons in the atom results in a local magnetic field at the nucleus. This hyperfine field can be expressed as a sum of contributions of individual electrons [1]:

$$\mathbf{B}_\mathrm{hf} = -\frac{\mu_0\mu_B}{2\pi}\sum_i \left(\frac{\mathbf{l}_i}{r^3} + \frac{\mathbf{s}_i}{r^3} - \frac{3\mathbf{r}(\mathbf{s}_i\cdot\mathbf{r})}{r^5} + \frac{8\pi}{3}\mathbf{s}_i\delta(\mathbf{r})\right)\,, \tag{1.2}$$

where the first term describes the field induced by electron orbital moment $\mathbf{l}$, while the remaining terms describe the field arising due to interaction with electron spin $\mathbf{s}$. The terms for dipole field adequately describe interaction with spin of electron within the dipole limit, whereas the last term gives the Fermi contact interaction. The contact field arises in cases when electron is present in a very close proximity to the nucleus (or inside the volume of nucleus), so that the dipole approximation breaks down, and additionally, relativistic effects have to be considered [1, 2]. Typically, the contact term is significant for atoms where the core s states are spin-polarized by d-s or f-s exchange with unpaired electrons in $3d$ or $4f$ shells; in case of $3d$ atoms, such as Fe, the contact field is usually the dominant contribution to the hyperfine field $\mathbf{B}_{\mathrm{hf}}$.

In non-magnetic systems, where all electrons are effectively paired in the atomic orbitals as well as within the chemical bonds, the hyperfine magnetic field is zero with a high precision (the non-zero effects, such as indirect nuclear spin-spin interaction, appear as terms in the second-order perturbation theory [2]). On the other hand, in magnetic systems the contributions of unpaired electrons are not compensated, yielding high value of magnetic hyperfine field at the nuclei. Then the very presence of such a hyperfine magnetic field is the key aspect for application of NMR spectroscopy to studying the magnetic materials [3]. The time-averaged value of hyperfine field for nuclei of paramagnetic atoms can be from several units of Tesla up to hundreds of Tesla, and additionally, transferred hyperfine field of lower magnitude can appear also at nuclei of neighboring non-magnetic atoms.

1.2 Hyperfine electric quadrupole interaction

For nuclei with spin $I > \frac{1}{2}$ the distribution of charge inside the nucleus deviates from the spherical one and is connected with presence of nuclear quadrupole (or higher order) electric moment, described as tensor $\mathbf{Q}$. The electric quadrupole moment $\mathbf{Q}$ interacts with gradient of electric field $\mathbf{E}$, which is generated by the surrounding electronic density and neighboring nuclei [1, 2]:

$$H_Q = \frac{e}{6}\mathbf{Q}\nabla\mathbf{E}\,. \tag{1.3}$$

Rotational symmetry and parity of the nucleus in the ground state dictate a special form of tensor $\mathbf{Q}$, allowing defining it with just one scalar component, Q [1]. The tensor of electric field gradient can then be considered as traceless,

$$\mathbf{V} = \nabla\mathbf{E} - \mathbf{1}\,\frac{1}{3}\mathrm{Tr}(\nabla\mathbf{E})\,, \tag{1.4}$$

and described by two parameters: the largest component V_{zz} and the asymmetry $\eta = \frac{V_{yy}-V_{xx}}{V_{zz}}$, with such a choice of coordinate system that $|V_{zz}| \geq |V_{yy}| \geq |V_{xx}|$. The electric quadrupole interaction is strongly influenced by the local symmetry: presence of 3-fold axis or higher symmetry causes η to be zero; moreover, for nucleus in cubic symmetry the electric quadrupole interaction does not influence the NMR spectrum.

1.3 NMR shifts

For non-magnetic materials in zero magnetic field, the hyperfine magnetic field effectively cancels out, and thus does not cause splitting of nuclear energy levels. Application of homogeneous magnetic field is then required to observe NMR, and the role of observable spectroscopic quantity is taken by subtle effects that change – locally – the value of the applied external field. When the external magnetic field is present, much weaker local magnetic fields are induced within the electron system and manifest as small changes of frequency in the NMR spectrum: the electronic response to the static field acts essentially as a "shielding", slightly shifting the resonance frequency from the value of bare, unshielded nucleus [1, 2],

$$\omega = \gamma \mathbf{B} = \gamma(1 - \sigma)\mathbf{B_0}\,. \tag{1.5}$$

In diamagnetic liquids and solids the effect is termed chemical shielding and when confronted with a shielding of the reference compound, the difference gives rise to so called chemical shift δ, usually expressed in ppm:

$$\delta = 10^6(\sigma_{\mathrm{ref}} - \sigma)\,. \tag{1.6}$$

Analogous terms in metals are called Knight shielding and Knight shift (K) and arise predominantly due to Fermi contact interaction with conduction electrons which are slightly polarized by the external magnetic field. The values of K are usually positive ("paramagnetic") and a few orders of magnitude larger than δ, thus often expressed as a percentage:

$$\omega = \gamma \mathbf{B} = \gamma(1 + K)\mathbf{B_0}\,. \tag{1.7}$$

In general, both quantities δ, K are tensors, so that the resonance frequency depends also on direction of the external magnetic field with respect the tensors' principal axes – such anisotropic properties correspond to the local symmetry of the crystal site with resonating nucleus.

2. Calculation of NMR parameters

Density Functional Theory (DFT) [4] belongs to the most important methods available for computations in condensed-matter physics, especially for many-body problems that are encountered when obtaining the electronic structures of solids. As in other self-consistent field (SCF) approaches, in DFT the many-body Schrodinger equation is rephrased as one-electron Kohn-Sham equations [5], which are then iteratively solved. Usually a reasonable set of approximations is applied to the original exact Hamiltonian, such as Born-Oppenheimer approximation and approximate potentials for the exchange and correlation (e.g., Local Density Approximation [4] or some variant of Generalized Gradient Approximation [6–8]). This self-consistent process yields, at its end, the electron density uniquely corresponding to the ground state for the studied many-body problem.

There exists a plethora of different DFT codes encompassing various approaches, parametrizations, and further approximations to tackle the solution to the SCF problem. In order to reach the hyperfine and related parameters, which are localized at or very close to the nucleus, it is natural to employ approaches that include description of the core electrons for all involved atoms, i.e., all-electron methods, also termed full-potential methods [9, 10]. This approach contrasts with pseudo-potential methods, where the core states of each atom are replaced by pre-calculated potentials [11, 12], which leads to notable increase in computational speed with almost no decrease of accuracy. Despite slower than the pseudopotential methods, the Full-Potential Linearized Augmented Plane Wave (FP LAPW) approach [13] is widely considered as one of the most precise electronic structure methods in solid state physics. In the FP LAPW scheme the volume of the crystal unit cell is divided into non-overlapping atomic spheres and an interstitial region, which differ by wave-functions used for description. Inside the atomic spheres the basis consists of "atomic-like" functions, while in the interstitial plane waves are used, and the solutions to the Kohn-Sham equations are expanded in such a combined basis set.

The DFT code that was used in all presented works is WIEN2k [14], which is based on FP LAPW, while employs additionally APW+lo (Augmented Plane Waves + local orbitals [15]) approach to be mixed with LAPW, allows additional local orbitals for better description of semi-core states [16], and various other features [17, 18]. Some of the spectroscopic parameters relevant for NMR can be evaluated from the calculated electron density and are often readily available, such as the hyperfine fields and electric field gradients, while obtaining other properties like NMR shifts requires additional and costly procedures.

In magnetically ordered materials the shape of experimental NMR spectrum is determined by the hyperfine magnetic fields at nuclei, while in non-magnetic materials the key parameter is NMR shift and (nuclear) magnetic dipole-dipole interaction. In both cases, if an appreciable electric quadrupole interaction is present, also the electric field gradients have to be considered, because strong electric quadrupole interaction can be decisive for the character and shape of the spectrum. In the following text we briefly describe how all these quantities are

calculated in the WIEN2k, what is their accuracy, and how various shortcomings can be overcome or circumvented.

2.1 Calculation of hyperfine magnetic fields

With electron density of the ground state available from a successfully converged SCF problem, it is relatively simple to calculate – for any specified nuclear site – the contribution due to the dipolar fields of electron spins or due to the orbital motion of the electrons. Since also the population matrices are calculated (and defined in the $|l, m, \sigma\rangle$ space, where l, m, and σ are orbital, magnetic, and spin quantum numbers) it is only a matter of obtaining mean value of a single particle operator $\hat{X}$ with Kohn-Sham eigenfunctions ϕ_i:

$$\langle\psi|\hat{X}|\psi\rangle = \sum_{E_i \leq E_F} \langle\phi_i|\hat{X}|\phi_i\rangle \ , \tag{2.1}$$

with the form of $\hat{X}$ according to orbital or spin-dipolar part in Eq. (1.2). Several approximations are applied [19]: first, the operator $\hat{X}$ is considered non-zero within the given atomic sphere only, second, the terms non-diagonal in l are neglected, and third, the relativistic mass enhancement is only approximately accounted for. All three approximations are relatively mild and perform well for localized magnetic moments of $3d$ and $4f$ compounds; on the other hand they would be less appropriate for, e.g., hyperfine field due to orbital moments in metals. The calculation of orbital and spin-dipolar hyperfine fields requires spin-orbit interaction to be included, but otherwise the time cost for such step is comparable to a single SCF iteration in a standard calculation.

For the Fermi contact term the process is even less demanding in terms of computational effort, however, it is less straightforward since the contact term expression (1.2) contains delta function, which diverges at point-like nucleus. Most DFT codes (including WIEN2k) do not consider finite size nuclei, but represent each nucleus with a point-like Coulomb potential. Since it can be shown [19] that the consideration of finite size of the nucleus is in fact not important for the hyperfine field, the situation is solved in the following way: the calculated electron (spin) density is averaged over a sphere with Thomson radius $r_T = \frac{Ze^2}{mc^2}$, which is typically an order of magnitude larger than the actual radius of the nucleus. The contact field is then integrated for such averaged spin density. A good agreement with experiments is reached for cases of nonmagnetic impurities in magnetic matrices [20–23], because the contact field at the impurity atom is dominated by spin-polarization of valence s states due to interactions with neighboring atoms. This approach works as well when evaluating isomer shifts for Mössbauer spectroscopy, where one also needs to calculate the electron charge density due to s-electrons within the nucleus [24].

Unfortunately, for magnetic atoms with unpaired $3d$ or $4f$ electrons, the contributions of core s states turn out to be significantly underestimated in comparison with experiments [25, 26]. This mismatch is, however, not caused by the applied mechanism with density smearing in the Thomson sphere, but it is clearly a failure of local density approximation to correctly describe the non-local d-s exchange interaction for the core states [19, 26]. To correct this shortcoming and make the calculated results applicable for comparison with experiments, we developed

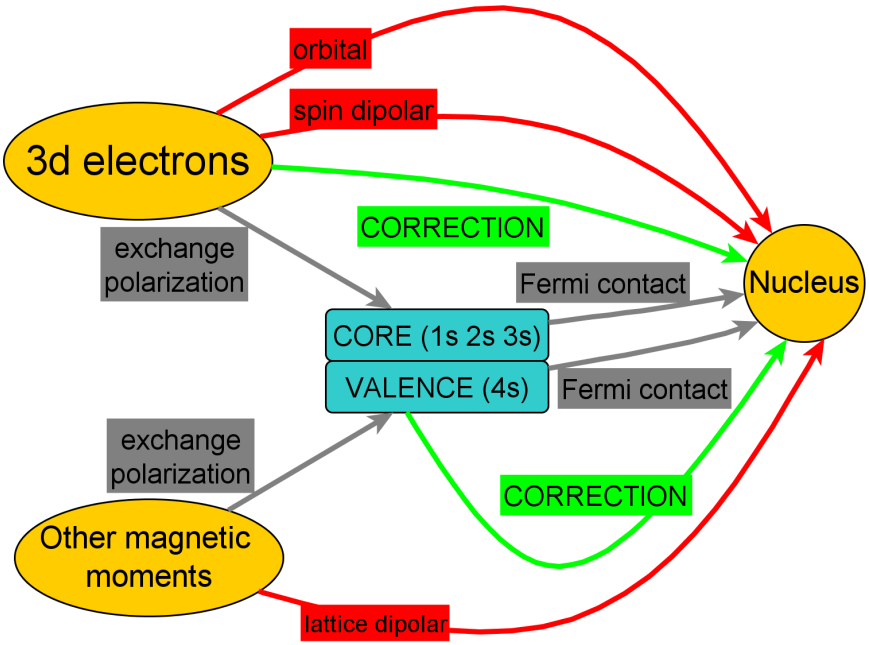

Figure 2.1: The scheme of sources of hyperfine magnetic field. The calculation of Fermi contact field (grey pathways) is circumvented by determining the core and valence contributions directly from magnetic moments (green pathways); the problematic exchange polarization is thus completely avoided.

an approach [VC1] that circumvents the problematic *d-s* exchange entirely (see Fig. 2.1) – for a specific atomic species, in our case Fe atoms.

The approach makes use of the fact that calculated atomic magnetic moments are in much better agreement with the experiments (e.g., neutron diffraction or magnetic measurements), in contrast to the underestimated hyperfine fields. Our analysis [VC1] for Fe in various magnetic compounds showed that the core contribution to the contact field scaled linearly with the magnetic moment of $3d$ electrons. Likewise, the valence contribution, which arises mostly due to transferred hyperfine field from neighboring atoms, scaled linearly with magnetic moment of valence $4s$ states of a given Fe atom. Therefore, our *ansatz* for reconstruction of the contact field was:

$$B_c = a_{3d} m_{3d} + a_{4s} m_{4s} \,, \tag{2.2}$$

where constants a_{3d} and a_{4s} were determined from fits to experimental ^{57}Fe NMR data. This correction to the Fermi contact term provided a suitable tool to explain and predict the values of the hyperfine fields on the Fe nuclei in various iron compounds containing ferric (and to some extent also ferrous) ions in the high spin configuration. Although the set of constants a_{3d} and a_{4s} relates to a specific type of atom only (in our case Fe, and for another species the process would have to be done separately), the application does not cost any extra computational resources and allows to obtain reliable contact hyperfine magnetic fields with precision better than 1 T (cf. 50 T, the typical value of contact field at ^{57}Fe).

2.2 Calculation of electric field gradients

The electric field gradient (EFG) tensor can be directly evaluated from the electron density of the ground state, again at no extra computational costs, since the EFG components are connected with charge density by integrals of the charge density $\rho(\mathbf{r})$ over the unit cell [27], e.g., for V_{zz} as:

$$V_{zz} = \int \rho(\mathbf{r}) \frac{2P_2(\cos\vartheta)}{r^3} \, \mathrm{d}\mathbf{r} \,, \tag{2.3}$$

where P_2 is the second-order Legendre polynomial. The $\rho(\mathbf{r})$ is represented by lattice harmonics $Y_{LM}(\mathbf{r})$, and in the LAPW method the integral is in practice a summation over occupied states [28]:

$$V_{zz} = \sum_{E<E_F} \sum_{lm} \sum_{l'm'} R_{lm} R_{l'm'} G^{Mmm'}_{Ll'} \frac{2P_2(\cos\vartheta)}{r^3} \,. \tag{2.4}$$

where R_{lm} are LAPW radial functions with angular momentum l or l', and G are the Gaunt coefficients [29]. For example when obtaining the component V_{zz}, we are interested in V_{20} component in the spherical representation of the EFG tensor, i.e., $L = 2$ and $M = 0$, and the number of non-zero contributions is then limited by G to combinations *p*-*p*, *d*-*d*, *s*-*d*, and *p*-*f*. This ability of the calculation to resolve EFG contributions according to particular l value is very important when interpreting the (dominant) sources of the EFG value in many practical cases [30, 31].

2.3 Calculation of chemical and Knight shieldings

While chemical shifts of molecules have been accessible for calculations for decades [32, 33], the implementation for solids has been delayed – among other complications – by the fact that the magnetic field breaks translational symmetry of the problem (leading to issues with gauge). For solids, within the projector augmented-wave (PAW) method [34], the gauge-including projector augmented-wave (GIPAW) approach [35] became successful for practical applications, especially when improved to be usable with nowadays ultrasoft-pseudopotentials in the pseudopotential DFT methods [36]. But for the family of APW/LAPW methods, and WIEN2k code in particular, the calculation of chemical shielding has been implemented only relatively recently [37–39]. The calculation involves enhancement of the basis set by local orbitals positioned at higher energies (unoccupied states), and then solving the eigenproblem for the original and six additional reciprocal k-point meshes (shifted along all six directions), for which the induced current as well as the magnetic susceptibility is obtained. The full chemical shielding tensor is then constructed straightforwardly from these seven calculations by integrating the current according to Biot-Savart law.

Compared to standard LAPW calculations, the chemical shielding calculations are significantly more demanding in terms of computational efforts. The difficulty further increases when the studied compound is a metal, which usually requires exceedingly dense sampling of the reciprocal space by the k-points. Additionally

for metals, the shielding due to polarization of conduction electrons, i.e., the Knight shielding K, has to be considered, as in metals it is the dominant source of shielding relevant for NMR spectroscopy. In order to determine K, explicit external magnetic field has to be applied in the calculation framework to obtain the induced contact hyperfine field due to electron spins, and likewise one has to calculate the spin-dipolar term. Again, the computational requirements are very high and make the application affordable for rather small or medium-size systems.

In NMR experiments the observed quantity, however, is the chemical (or Knight) shift, i.e., the difference in shielding between the measured and the reference compound. Therefore, in order to allow for comparison with experiment, one should – in principle – calculate also such NMR reference compound. This is usually not a well suited approach, since it increases the uncertainty of the final figures, and additionally, the reference compounds are quite often liquids, or solids with peculiar structures (e.g., nitrates with large unit cells and containing crystal water molecules) exceeding in complexity the studied compound. Much more convenient and reliable approach [40–42] involves matching the calculated shieldings with experimental shifts of several compounds using a linear regression (with slope usually very close to 1).

2.4 Role of anisotropic interactions

When attempting to model the experimental NMR spectrum, one now has all relevant spectroscopic parameters available for calculation with reasonable precision:

- the total magnetic field – in form of hyperfine magnetic field for magnetic systems, or external magnetic field modified by the NMR shielding for non-magnetic systems,
- and the electric field gradient for electric quadrupole interaction (if present).

Nevertheless, in very complex cases with many non-equivalent atomic positions the experimental spectra may consist of a high number of spectral lines, which may be overlapping or insufficiently resolved. The spectroscopic parameters of different lines in the experimental spectrum then can be simply too similar – compared to the precision of the calculated parameters – to allow for unambiguous assignment of the spectrum, i.e., to match each individual spectral line to its respective atomic position using the calculated parameters. In such cases there is a need for additional parameters to be compared, which can be for instance the anisotropies of the relevant quantities, namely the anisotropy of hyperfine magnetic field and the anisotropy of chemical or Knight shielding.

We developed such an approach employing the anisotropy of hyperfine interaction in Ref. [VC2] and tested it for the ordered spinel structure of lithium ferrite. In spite of lithium ferrite being a relatively simple compound with only two crystallographically non-equivalent Fe sites (tetrahedral and octahedral), two of the five lines in the zero-field experimental ^{57}Fe NMR spectrum cannot be unambiguously interpreted solely from the experiment: the lines have the same integral intensity and the corresponding Fe sites differ only by the orientation of the local axes with respect to the vector of magnetization. In other words, the two sites are crystallographically equivalent but magnetically non-equivalent,

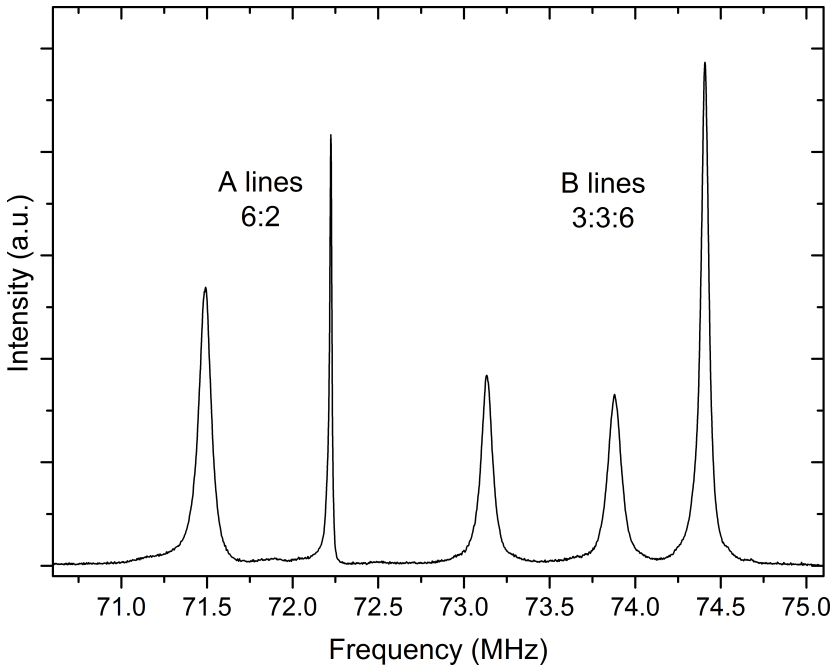

Figure 2.2: NMR spectrum of ordered lithium ferrite measured at 4.2 K in zero magnetic field. In the octahedral sub-spectrum (B lines) the two lines at 73.134 and 73.879 MHz are impossible to assign solely from the NMR experiment.

and thus can be distinguished only by the anisotropic part of hyperfine magnetic interaction, which is briefly described below.

The total local magnetic field at ^{57}Fe nucleus is mainly given by the hyperfine field with the Fermi contact, the orbital, and the spin-dipolar contributions, from which only the Fermi contact term is purely isotropic, i.e., its absolute value does not depend on direction of electronic magnetization. Additionally, atomic moments in the surrounding lattice also contribute to the local field by their (classical) dipolar fields; this contribution to the local field is purely anisotropic and can be straightforwardly determined by summation within a sufficiently large Lorentz sphere. The total local field then consists of isotropic and anisotropic part,

$$\mathbf{B}_{\mathrm{loc}}(\mathbf{n}) = \mathbf{B}_{\mathrm{iso}} + \mathbf{B}_{\mathrm{anizo}}(\mathbf{n})\,, \tag{2.5}$$

and for a given direction of magnetization $\mathbf{n}$ a single crystallographic site – depending on its local symmetry – may give rise to one or more lines in the spectrum.

Experimentally, one can observe situations for values of $\mathbf{n}$ different from the easy direction by recording NMR spectra of a single crystal under application of external magnetic field, sufficient to rotate the vector of magnetization from the easy direction into the desired direction $\mathbf{n}$ [43]. In the calculations, the direction of magnetization can be arbitrarily specified as a hkl vector in the unit cell, whenever the spin-orbit interaction is considered for a spin-polarized case. Thus, confronting the behavior of experimental and calculated spectra for varying $\mathbf{n}$ yields extra information: the sites can be additionally distinguished according to anisotropy of their hyperfine magnetic fields.

The ^{57}Fe spectrum of tetrahedral A sites in Li ferrite is clearly understood [43] from the NMR experiment by simple symmetry considerations, in fact already without the application of external magnetic field. All eight tetrahedral Fe sites

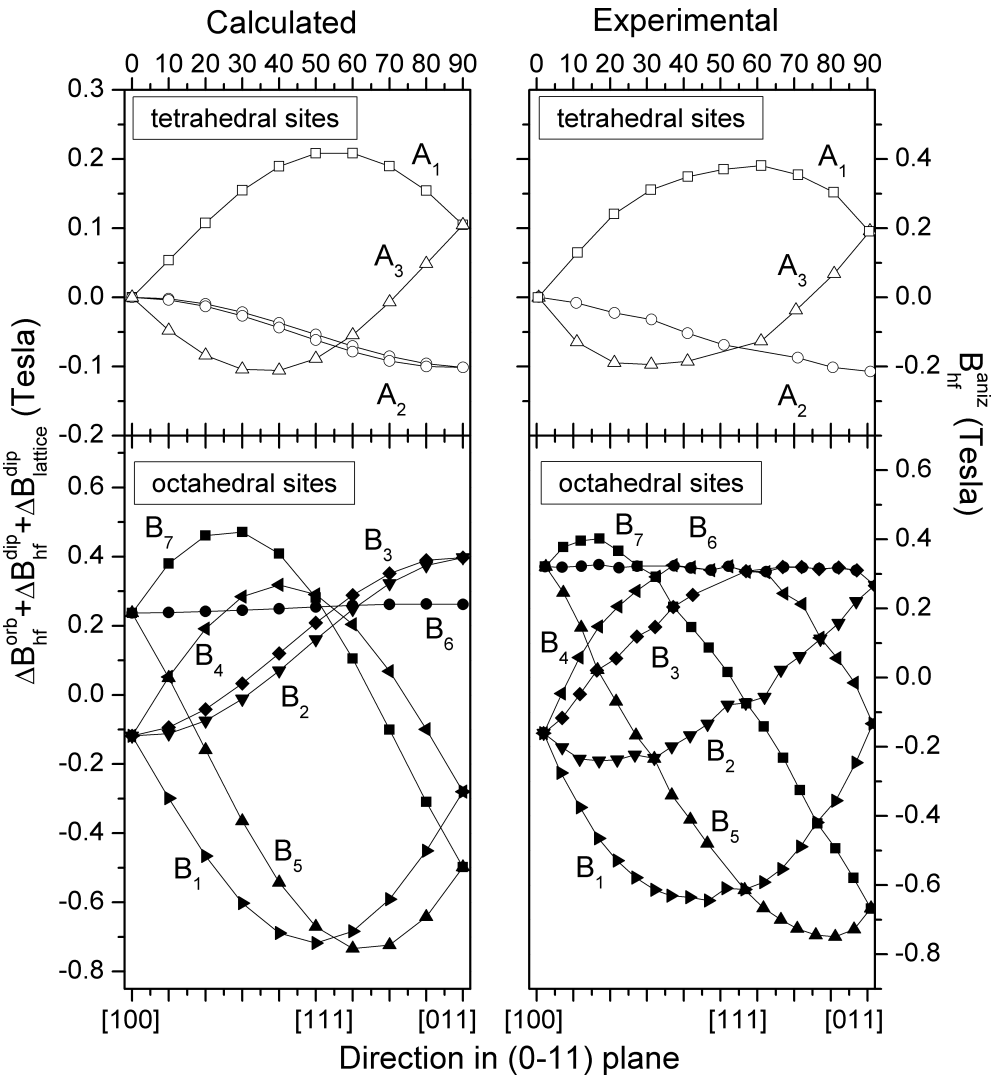

Figure 2.3: The comparison of calculated and experimental ^{57}Fe hyperfine field anisotropies in ordered lithium ferrite. The experimental fields were derived from angular dependences of ^{57}Fe NMR spectra measured at 4.2 K in external magnetic field 0.266 T [43]; our calculations modeled the experiment for directions of magnetization within $(0\bar{1}1)$ plane. Both experimental and calculated fields were adjusted by subtracting their isotropic parts. Adapted from Ref. [VC2]

possess trigonal symmetry with axis oriented along $\langle 111 \rangle$, i.e., there are four groups – each containing two tetrahedral sites – with local axes along either the [111], $[\bar{1}11]$, $[1\bar{1}1]$, or $[11\bar{1}]$ direction. Concurrently, the easy axis of magnetization in lithium ferrite lies in one of these directions. Therefore, one of the four groups of tetrahedral sites has the local axis parallel with the easy direction of magnetization, while for the other three groups they are not parallel: the vectors of these directions are intersecting (forming an angle of ~ 70.5 degrees). This leads to a fundamental difference in how the resonance frequencies in tetrahedral subspectrum depend on the direction of magnetization, and consequently causes these two types of tetrahedral sites to be easily distinguishable, yielding the 2:6 line ratio in zero-field ^{57}Fe spectrum in Fig. 2.2.

Such simple situation is not found for the octahedral spectrum, which is split

into three lines 3:3:6 for the easy direction of magnetization and remains ambiguous even when the direction of magnetization is changed by the external field. Specifically, the spectral lines at 73.134 and 73.879 MHz in Fig. 2.2 cannot be unambiguously identified with the corresponding six crystal sites (3:3). Again as in the tetrahedral case, the frequencies of octahedral sites change according to the behavior of their hyperfine field anisotropy, however, this time the differences are more subtle: there is no distinguishing symmetry element present and the sites differ only by the numerical value of the anisotropy. This leads to a deadlock: if the hyperfine tensor was known, the values of hyperfine field anisotropy could be directly calculated and lines assigned to sites. However, the tensor cannot be determined uniquely (ambiguity in sign of one of the parameters) from the experiment because of the lines not being unambiguously assigned. In Ref. [VC2] the situation for octahedral sites was remedied by calculating the anisotropy tensor from DFT, which allowed to match the calculated and experimental data [43], and finally assign also the octahedral lines to their corresponding Fe sites (Fig. 2.3).

The approach employing the anisotropy of hyperfine interaction thus opens another path to assign and interpret the experimental spectra, although this benefit comes at a cost of much more demanding experiments. In order to measure the angular dependences of NMR spectra, naturally one should use a single crystal sample, as well as appropriate NMR experimental setup. And likewise, the calculations and the following analysis may also become quite extensive.

3. NMR & DFT: Applications to magnetic and non-magnetic solids

This chapter presents several publications where we applied the approach of comparing the NMR spectroscopy experiments (in three of the cases also the Mössbauer spectroscopy experiments) with results obtained from calculated DFT models. The topic of the studied systems concerns mainly magnetic solids, namely iron oxides, for which the key parts of the NMR-DFT comparison have been developed [VC1, VC2].

First we present two studies related to valence states of Fe atoms in hexaferrites, where both benefits of the NMR-DFT comparative approach, mentioned in the introduction, are demonstrated: the calculations serve as a helpful tool for interpretation of experiments and conversely the experiment is used to justify the calculated results. Other hexaferrite studies follow, as well as works concerned with magnetite and various magnetic ferrites, and the chapter is completed by application of the comparative approach to several non-magnetic solid-state systems.

3.1 Hexagonal ferrites

Hexagonal ferrites (hexaferrites) are magnetic oxides of iron and atoms of alkali earth metals (Ba, Sr, Pb) or lanthanides (sometimes termed large cations), often accompanied by substitutions of various elements (Co, Al, ...). The industrial and technological importance of hexaferrites as permanent magnets, in magnetic recording, and wide range of high-frequency and electrical devices perhaps overshadows their other interesting properties discovered recently, such as promising multiferroic behavior [44, 45] or outstanding microwave absorption in form of various composites [46, 47].

The hexagonal ferrites consist of stacked structural blocks along the hexagonal axis; there are three possible structural blocks, T, R, and S. According to the type of block used, the compounds can be organized into two main families: first, containing R and S blocks only, where the simplest R-S stacking yields the M-type structure, and second, built with T and S blocks, with Y-type hexaferrite (T-S stacking) being the simplest representative. More complex structures then can be derived (and more importantly also synthesized) by altering the sequence of the building blocks or combining the two families together [48].

The magnetic structure of hexaferrites is ferrimagnetic, with moments of neighboring Fe atoms along the hexagonal axis being mutually antiparallel. Hexaferrites display high magnetic anisotropy of either easy axis character (mostly M-type and related structures) or planar/conical type (usually Y-type and derived structures) [48]. Their magnetic properties, especially the magnetocrystalline anisotropy, are sensitive to magnetic and valence states of Fe atoms [49], and can be also influenced by various cationic substitutions (e.g., Co^{2+}). The determination of Fe valence states in hexaferrites was also one of the main topics in the next two presented papers.

The structure of hexagonal ferrites contains five or more crystallographically

non-equivalent Fe sites, which are also magnetically equivalent when the magnetization is along the hexagonal axis, but may become split for other cases, e.g., for planar hexaferrites. Since the nuclear spin of ^{57}Fe isotope is $1/2$, the electric quadrupole interaction does not apply in NMR, and each non-equivalent Fe site then usually gives rise to one spectral line in the ^{57}Fe NMR spectrum. The experimental NMR spectra of hexaferrites may become difficult to interpret: the complexity of their spectra steeply rises with increasing number or non-equivalent sites in the structure, as well as for ferrites with planar magnetic anisotropy where the anisotropy of hyperfine interaction may affect the shapes of spectral lines or cause splitting. With exception of the simplest and well-studied M-type hexaferrite, the assignment of all NMR spectral lines is often incomplete [50, 51]. For other related hyperfine methods, such as Mössbauer spectroscopy, already the M-type structure with five iron sublattices implies five overlapping sextets, whose analysis can be a complicated problem, and more complex structures are usually beyond the method's resolution [52, 53].

Localization of valence electron in hexaferrites with mixed valence

Good examples of such more complex structures are strontium W-type and X-type hexagonal ferrites, on which we focused in the study by ^{57}Fe NMR and Mössbauer spectroscopies and DFT calculations in Ref. [VC3]. Both ferrites are composed of the same set of building blocks – R and S – as the simplest M-type structure ("SrM", $SrFe_{12}O_{19}$, space group $P6_3/mmc$), which has the stacking sequence R-S. The stacking sequence of the W-type structure ("SrW", $SrFe_{18}O_{27}$, space group $P6_3/mmc$) is R-S-S and the X-type structure can be considered as a sum of M- and W-type, yielding R-S-R-S-S stacking ("SrX", $Sr_2Fe_{30}O_{46}$, space group $R\bar{3}m$).

Both SrW and SrX are mixed-valence ferrites, i.e., contain both (nominally) ferric and ferrous ions, and thus our aim was to study the specifics of the valence charge: whether the valence charge is localized in the form of Fe^{2+} and which Fe crystal sites are involved. The applied spectroscopic methods are sensitive to the valence state of Fe atoms: value of isomer shift, which is obtained from Mössbauer spectra, can be attributed to the given valence state, whereas NMR detects Fe^{2+} indirectly as a missing intensity in the ^{57}Fe spectrum from Fe^{3+} atoms. However, first the NMR and Mössbauer spectra had to be interpreted (their lines assigned to crystallographic Fe positions), for which the DFT calculations were utilized. Moreover, the valence states of iron atoms were also determined from the ground state obtained in the electronic structure calculations, and thus the calulated valences were used together with the experimental results to identify the Fe^{2+} sites [VC3].

The five Fe sublattices in the M-type structure are occupied by nominally ferric ions and are labeled as $12k_{\mathrm{VI}}$, $4f_{\mathrm{IV}}$, $4f_{\mathrm{VI}}$, $2b_{\mathrm{V}}$, and $2a_{\mathrm{VI}}$, where the labels indicate the multiplicity, Wyckoff symbol, and oxygen coordination ("IV" and "VI" are tetrahedral and octahedral, respectively, while "V" denotes hexahedral site, usually termed bipyramidal). Accordingly, the ^{57}Fe NMR spectrum of SrM consisted of five narrow and well separated resonance lines, and since its interpretation is well known [54], the lines could be assigned to the respective sublattices, as depicted in Fig. 3.1. The hyperfine magnetic fields, measured by NMR as well as Mössbauer, were in a very good agreement with the calculated values (using corrected contact fields via the method described in [VC1]). Likewise, the calculated values of EFG

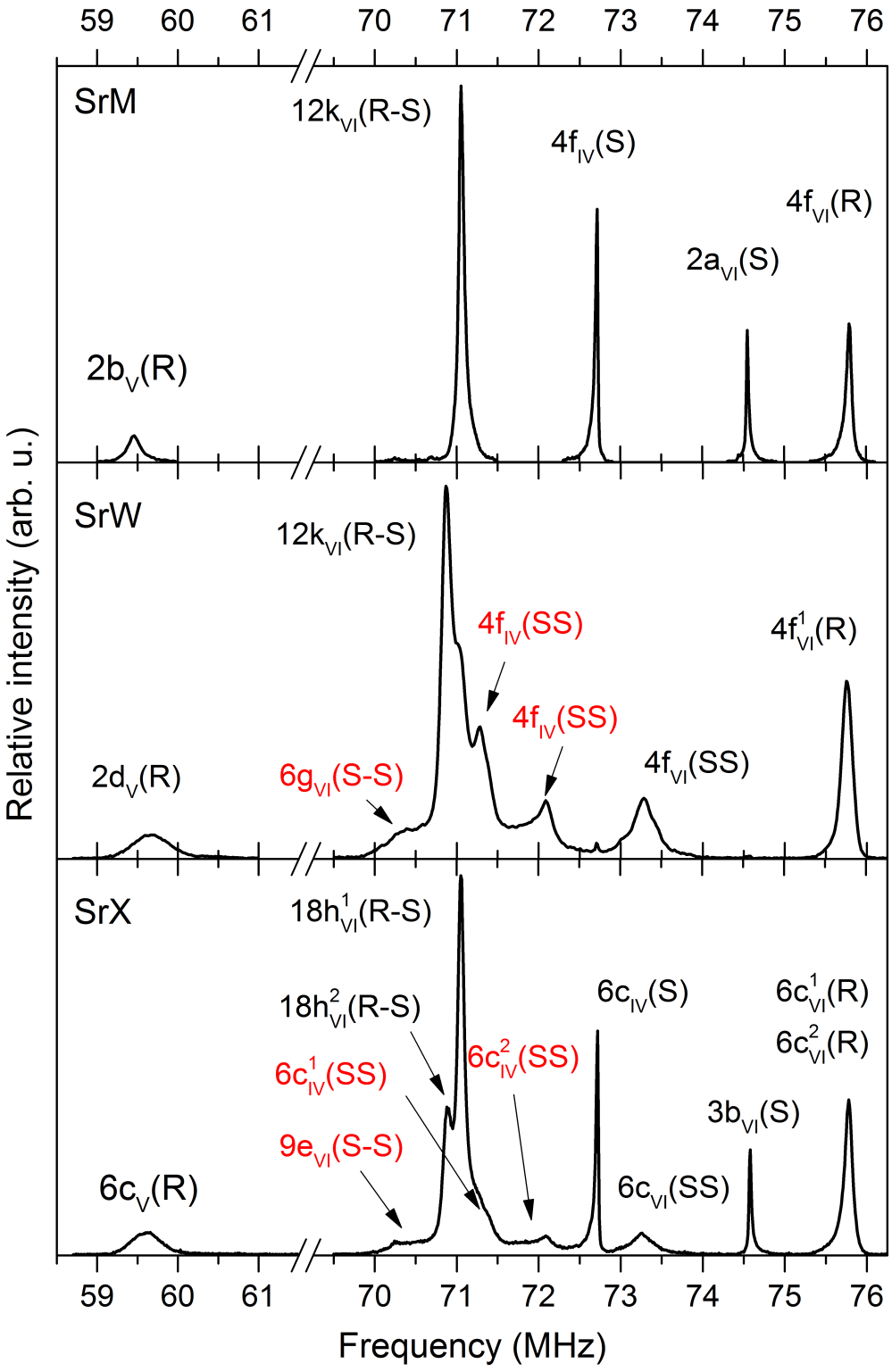

Figure 3.1: Experimental ^{57}Fe NMR spectra of M-type $SrFe_{12}O_{19}$, W-type $SrFe_{18}O_{27}$, and X-type $Sr_2Fe_{30}O_{46}$ with spectral line assignment indicated. The lines labeled in red were only assigned by employing the DFT calculations. Partially adopted from Ref. [VC3].

on Fe nuclei basically matched the experimental quadrupole splittings – for ^{57}Fe these are observed in Mössbauer only. As expected, the valence states of Fe atoms (obtained by Atoms in Molecules method [55]) were essentially Fe^{3+}, which was also confirmed by the measured isomer shifts.

For SrW hexaferrite with seven Fe sublattices, the interpretation of the ^{57}Fe NMR experiment is already incomplete and only four of the seven lines in the ^{57}Fe NMR spectrum can be directly assigned to sites upon their resemblance with SrM ^{57}Fe NMR spectrum, integral intensities, and response to external magnetic field [56]. The Mössbauer spectra and DFT calculations helped to resolve the issue: the connection of three sites in the S-block part of the structure, $6g_{\mathrm{VI}}$, $4f_{\mathrm{IV}}$, $4e_{\mathrm{IV}}$, with three unassigned lines in the NMR spectrum became possible by comparison with hyperfine fields from NMR and also by comparing EFGs from Mössbauer spectra with those calculated by DFT.

Similar obstacles with interpretation were encountered for SrX structure with its eleven Fe sublattices. While again some of the lines could be assigned – by literally matching these with analogous sites and spectral lines of SrM and SrW hexaferrites – remaining three lines were once more assigned using the calculated hyperfine fields.

All Fe atoms in SrM are in high-spin ferric state Fe^{3+}, but both SrW and SrX contain also some ferrous atoms Fe^{2+}, formally being $SrFe^{2+}_2Fe_{16}O_{27}$ and $Sr_2Fe^{2+}_2Fe_{28}O_{46}$, respectively. The question of localization of Fe^{2+} in one or more crystallographic positions was thus mainly addressed in the Ref. [VC3]. From the analysis of NMR line intensities, isomer shift in the Mössbauer spectra, and calculated valence in the DFT we concluded that the minority electron tends to be localized in $6g_{\mathrm{VI}}$ and $4f_{\mathrm{VI}}$ of the SrW structure, and in $9e_{\mathrm{VI}}$ and $6c_{\mathrm{VI}}$ of the SrX structure. All these sites are located in between the two neighboring S blocks. Such behavior can be understood given the fact that the S block possesses spinel-like structure, $2Fe_3O_4$, and is thus more inclined to incorporate the extra valence electron, compared to R block, $SrFe_6O_{11}$.

Related issue of valence charge compensation was the subject of another hexaferrite study [VC4], concerning substituted SrM. There are only ferric Fe present in the SrM, however, when the divalent strontium is replaced by a trivalent cation, the charged substitution is compensated by change of valence of some of the Fe atoms. It has been shown [57–59] that in lanthanum M-type hexaferrite (LaM), where La is formally trivalent, at low temperatures the compensation occurs via localization of minority electron at octahedral 2a sites, forming $Fe^{2+}(2a)$. Such process is accompanied by a notable increase of magnetocrystalline anisotropy, compared to LaM at room temperature or to anisotropy of SrM (Fig. 3.3 left).

The charge localization in LaM (and also in Nd- and Pr-substituted cases) and its influence on magnetocrystalline anisotropy were studied by combining DFT calculations and ^{57}Fe NMR spectroscopy [VC4]. This time the DFT calculations were not employed to mainly provide help with interpretation of NMR spectra, but we utilized the second "branch" of the relationship between the experiment and calculations: the experiments justified the correctness of our DFT model in describing the localized state. The credibility of the ground state obtained by DFT was important because of employing DFT+U approach [60, 61] and because of dealing with calculation of magnetocrystalline anisotropy energy; both issues

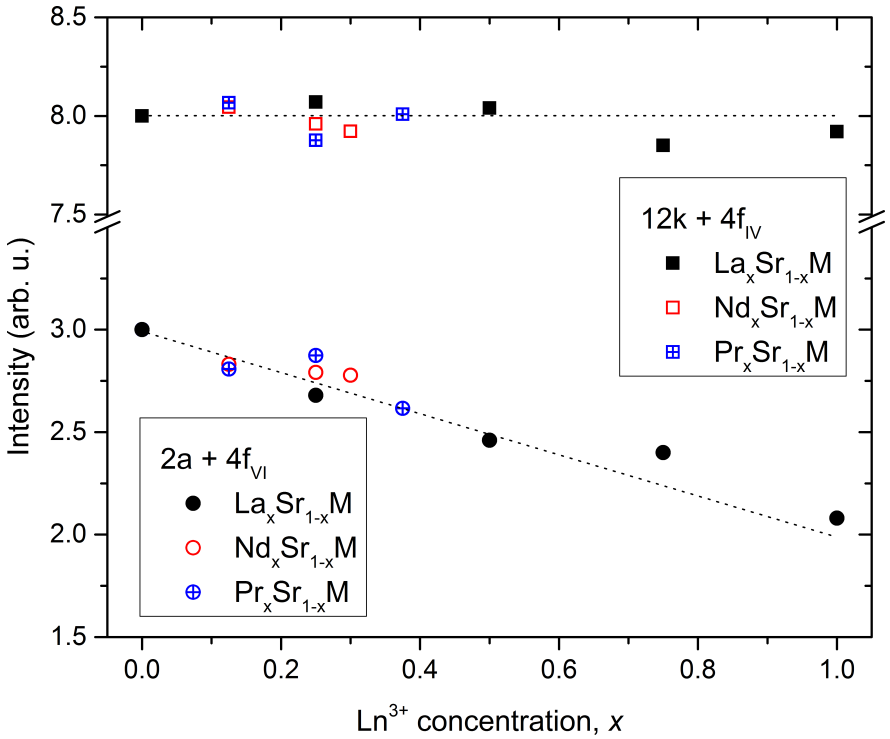

Figure 3.2: Integral intensities of parts of ^{57}Fe NMR spectra in pure and doped SrM and LaM. The dependence of intensities on the concentration of trivalent large cation supported the conclusion that Fe^{2+} localized in octahedral 2*a* sites. Adopted from Ref. [VC4].

are described below in a bit more detail.

When calculating magnetic ferrites, the proper description of Fe 3*d* states is essential and one of the successful, albeit simple approaches is the DFT+U method [60]. The idea is to treat the strong on-site Coulomb interaction of localized 3*d* states, which are not correctly described by the generalized gradient approximation (GGA), with an additional Hubbard-like potential – its strength being parametrized by on-site Coulomb interaction U and site exchange J. For instance, without application of a reasonable U the calculated ground state of some hexaferrites is incorrectly metallic [62], and thus the application of such potential, usually in a form [61] of $U_{\text{eff}} = U - J$ and strength of several eV (4.5 eV in our calculations), is a routine procedure to remedy the shortcoming of GGA exchange-correlation potential.

On the other hand, application of the DFT+U approach may produce additional local energy minima for the SCF process [63–65] and in case of complex structures there is a danger that the calculation converges into a stable state which is not the real ground state. When more than one such stable self-consistent solution is obtained in DFT+U, the proper one has to be chosen – usually according to the lowest total energy, or the justification can also be provided by comparison with suitable experiments; both apply to our case.

In La-, Nd-, and Pr-doped Sr hexaferrites at low temperatures the intensity of ^{57}Fe NMR line corresponding to octahedral 2*a* sites diminishes proportionally to the concentration of the trivalent cation (see Fig. 3.2). The presence of La^{3+} (as well as Nd^{3+} or Pr^{3+}) induces Fe^{2+} in the 2*a* sites, which is accompanied by a

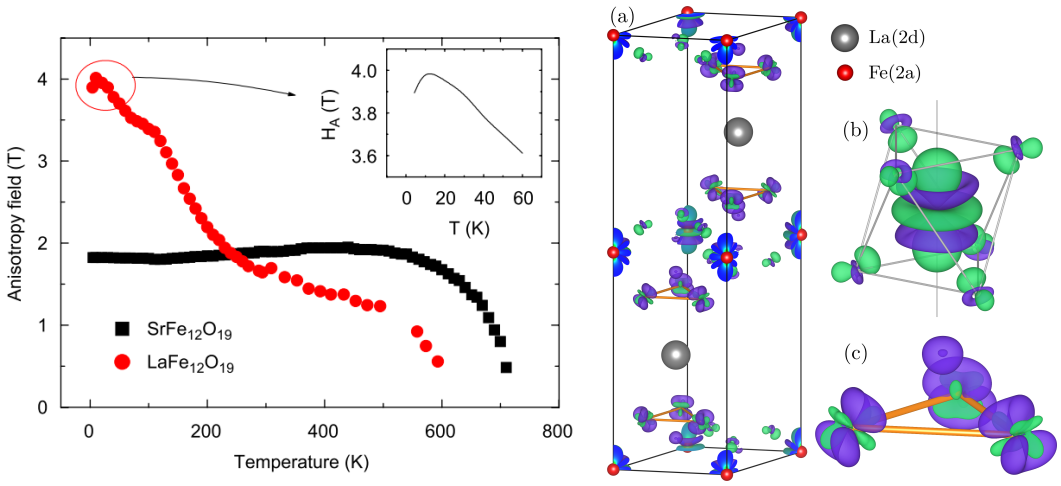

Figure 3.3: The experimentally observed temperature dependence of anisotropic fields [58] (left panel) was modeled and satisfactorily explained by the calculated magnetocrystalline energy. In LaM at low temperatures the Fe^{2+} localizes in $2a$ sites, as documented by differences in charge density in a 3D plot (right panel, b) and strongly contributes to the anisotropy; with increasing temperature the minority charge delocalizes, mainly within 12k and 2a sites and leads to reduced anisotropy. On the other hand, there is no such process present in SrM as documented by the constant temperature dependence of its anisotropy. Adopted from Refs. [58] and [VC4].

significant reduction of the hyperfine field at ^{57}Fe nuclei. The NMR line intensity is thus effectively reduced by the amount of Fe^{2+} and can be utilized to monitor Fe^{2+} concentrations. The linear decrease of Fe($2a$) NMR intensity indicates that the distribution of Fe^{2+} in the $2a$ sublattice is rather static at low temperatures without significant fast electron hopping. Therefore, within the $2a$ sublattice there are well defined ferric and ferrous ions and their arrangement at low temperatures does not change significantly.

Such a scenario observed in ^{57}Fe NMR experiment was searched for by the DFT+U calculations. Our aim was to obtain the "localized" solution, i.e., Fe^{2+} in $2a$, as well as the "delocalized" solution – with different (and at the time unknown) way of compensating the extra valence charge – and to use these electronic structures to evaluate magnetocrystalline anisotropy and compare it with experiment (see Fig. 3.3 left).

In order to calculate the magnetocrystalline anisotropy energy E_{MA}, it is useful to utilize so called force theorem approach [66] and evaluate E_{MA} as the difference between the total energies of calculations with different directions of magnetization. In the M-type hexaferrites with uniaxial character of anisotropy, such suitable directions are the hexagonal axis (001), which is the easy axis of magnetization, and any direction in the hexagonal plane, e.g., (100). For these hexaferrites the anisotropy is dominated by single-ion contributions of Fe atoms due to spin-orbit interaction and yields anisotropy constant $K_1 = 0.36$ and 0.09 MJ.m^{-3} for localized and delocalized LaM, respectively, and 0.18 MJ.m^{-3} for SrM. Although these values are about half of the experimental values [67], they are in excellent agreement with the temperature behavior of anisotropy field of LaM and SrM in experiments [58].

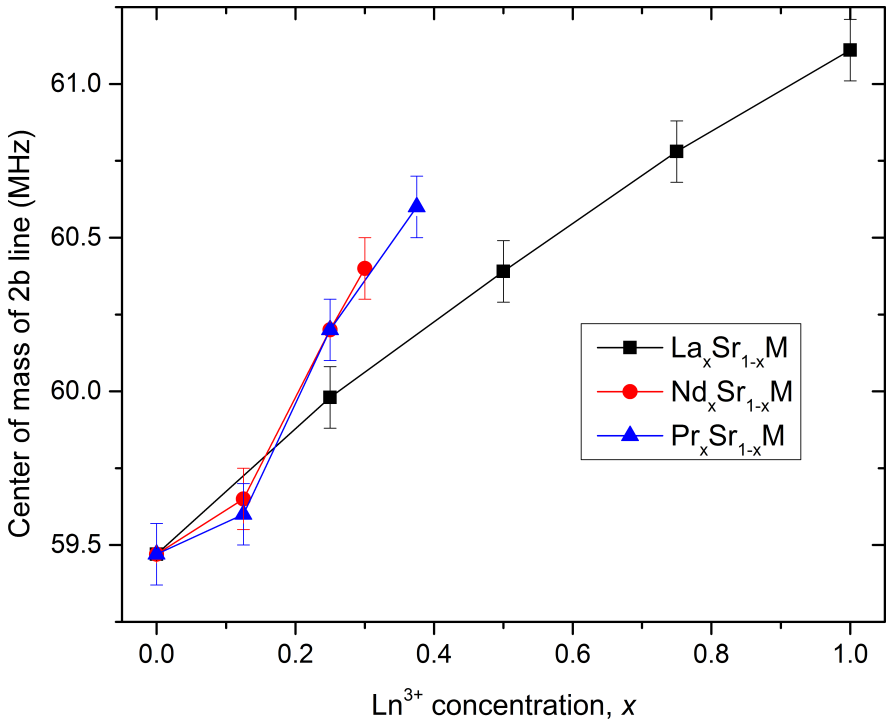

Figure 3.4: Frequency shift of the $2b$ line resonance in dependence on the concentration of trivalent large cation. Adopted from Ref. [VC4].

Moreover, the spin-orbit interaction can be arbitrarily enabled or disabled for any atomic species in the structure, which allows to evaluate the contributions of individual Fe sublattices to E_{MA}. We thus confirmed that the bipyramidal $\mathrm{Fe}^{3+}(2b)$ causes large anisotropy, nevertheless, its single-ion contribution is constant in both LaM solutions, as well as in SrM. Whereas the key role for the increase of E_{MA} at low temperatures is played by $\mathrm{Fe}^{2+}(2a)$ and to some extent by $\mathrm{Fe}^{3+}(12k)$, see Fig. 3.3 right. When the localization into octahedral 2a sites in LaM takes place, the contribution of $\mathrm{Fe}^{2+}(2a)$ is responsible for about 70 % of the total E_{MA}. On the other hand, at higher temperatures, the delocalized scenario is realized and the minority electron is smeared over multiple Fe sites, partly again $2a$, but mostly $12k$, negative contribution of which effectively reduces the total magnetocrystalline anisotropy.

The selection of large cation affects strongly not only the magnetic and other physical properties of hexagonal ferrites, but manifests also through relatively subtle effects in the ^{57}Fe NMR spectrum. One could expect that the nearest Fe neighbor to the large cation site, the bipyramidal Fe($2b$) site, should be the most affected site by the substitution of large cation. This is manifested by the hyperfine field of Fe($2b$) visibly increasing with increasing concentration of large cation that substitutes Sr, as observed from frequency shift in NMR spectra (Fig. 3.4). But surprisingly, the changes are not due to extra valence charge brought by substitution of La^{3+} for Sr^{2+}, but rather due to changes of geometry, to which the hyperfine field of bipyramidal site is particularly sensitive. The perturbation of local structure can be most probably caused by the different atomic size of the large cations: the calculated atomic volume of La^{3+} is about 13 % larger than that of Sr^{2+}.

The effect of large cation size on neighboring Fe can be well observed in the ^{57}Fe NMR spectra of Ba and Sr M-type hexaferrites, where the hyperfine field of Fe(2*b*) differs by about 0.9 T. The remaining four Fe sublattices have essentially the same positions in ^{57}Fe NMR spectra, hence their hyperfine fields are almost unchanged by the type of large cation. The explanation of this difference in BaM and SrM, and its connection to local and lattice geometry, unexpectedly followed from our analysis of lattice deformations on calculated hyperfine magnetic fields [VC5]. Due to larger ionic size of barium, the neighboring bipyramidal site is more expanded compared to SrM, which leads to weaker effect of Fe-O covalency and lower hyperfine field.

Originally, the analysis [VC5] of how the lattice deformations influence the hyperfine fields was motivated by non-uniform shifts found out in ^{57}Fe NMR spectra of SrM oriented thin films [68]. In principle, for samples with reduced dimensions such as nanoparticles or thin films, the values local fields at ^{57}Fe nuclei may differ from those in a bulk single crystal due to presence of demagnetizing field. As a consequence, the spectral lines should be uniformly shifted: those with magnetization parallel to the total magnetization to higher frequencies and vice versa. Our analysis brought a deeper insight into the connection of lattice deformations and observed hyperfine fields and by studying dependences of calculated hyperfine fields on changes of volume and c/a ratio of the lattice parameters, we rejected the conjecture that the observed shifts can be simply explained by lattice mismatch with the substrate. Some other structural defect in the SrM thin film has to be affecting the hyperfine field of each iron site differently.

Atomic arrangement in planar multiferroic hexaferrites

The NMR spectroscopy and DFT calculations were employed to study the local structures of other hexagonal ferrites – in the family of Y-type, planar hexaferrites. Mixed Ba/Sr Zn_2Y-type was one of the first hexaferrites where magnetoelectric properties were discovered, notably with transition temperatures above the room temperature [44].

The structure of Y-hexaferrite consists of T-S block stacking and besides four octahedral sites the structure contains two tetrahedral sites: one in the T block and the other in the S block. Since Zn atoms strongly prefer tetrahedral environment, the octahedral sites are fully occupied by Fe, while the tetrahedrons contain both Fe and Zn. The Zn/Fe distribution between blocks can be described by parameter γ: the S block contains Zn_γ and the T block contains $Zn_{1-\gamma}$. The distribution of zinc atoms is a one of the key parameters for the ferroelectricity and many other properties [44, 69, 70], with $\gamma = 0.5$ expected to be the most suitable for magnetoelectricity. Therefore, our aim was to study experimentally the Zn distribution in Ba- and Sr-Zn_2Y hexaferrites by means of ^{57}Fe and ^{67}Zn NMR. The role of DFT calculations was mainly to interpret the measured NMR spectra. The viability of such approach was shown in Ref. [VC6], where already a rough DFT model allowed us to assign the two components in ^{67}Zn NMR spectrum to the two respective Zn sites in the T and S block of the Y hexaferrite structure. In the ^{67}Zn spectra, simulated from calculated electric field gradients and hyperfine magnetic fields, the line originating from Zn in S block and T block could be clearly distinguished.

Further improving on the DFT model in Ref. [VC7] provided finer resolution of

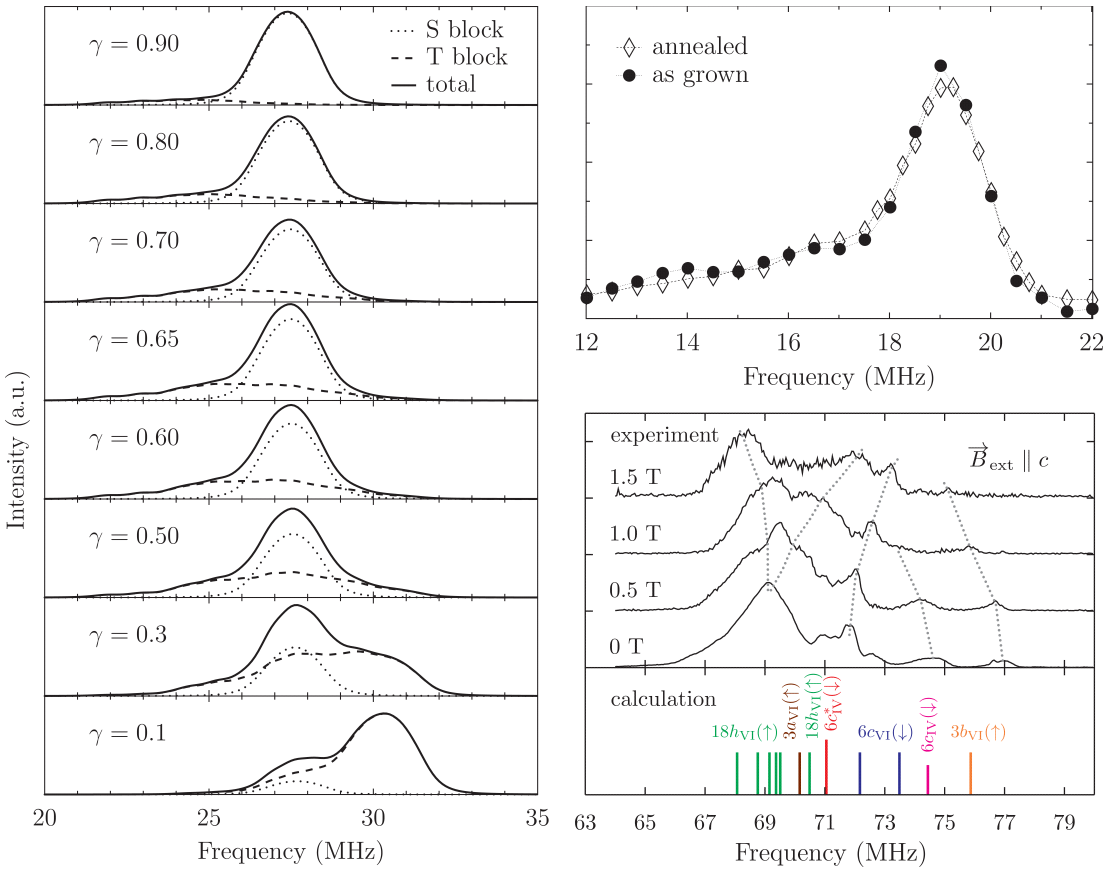

Figure 3.5: The ^{67}Zn NMR spectra simulated for various values of parameter γ (left) allowed determining the Zn distribution in the experimental NMR spectra (top right). Bottom right: the application of external magnetic field and calculations of hyperfine magnetic fields lead to assignment of ^{57}Fe NMR spectra in barium Zn_2Y-ferrite and to evaluation of parameter γ. Adopted from Refs. [VC6–VC8].

the parameter γ (Fig. 3.5 left) and its more reliable determination. Interestingly, the hyperfine field for Zn in the S-block was relatively unaffected by value of γ and the frequency of the corresponding ^{67}Zn resonance line kept constant, while the T-block Zn resonance shifted significantly when γ was changed. The shape of the simulated spectrum thus related to the distribution of Zn in the structure and could be used to determine the value of $\gamma \sim 0.65$ for the experimental spectrum – by a simple comparison. The heat treatment lead to only a minuscule differences in the measured spectra (Fig. 3.5 top right).

In contrast to zinc, the ^{57}Fe spectra are much more complex, containing signals from six different Fe sublattices, some of which are further split due to Zn/Fe disorder within both tetrahedral sites. Reasonable interpretation of ^{57}Fe NMR spectrum was reached in pure Ba-Zn_2Y hexaferrite [VC8], where complications from the Ba/Sr disorder were avoided. Application of external magnetic field in the NMR experiments allowed to separate the Fe crystal sites according to the orientation of their magnetic moments: for atoms with moments parallel to the total magnetization their nuclear resonance shifts to lower frequencies and vice versa. Together with calculation of hyperfine fields on ^{57}Fe nuclei we were eventually able to assign the experimental ^{57}Fe NMR spectrum (Fig. 3.5 bottom

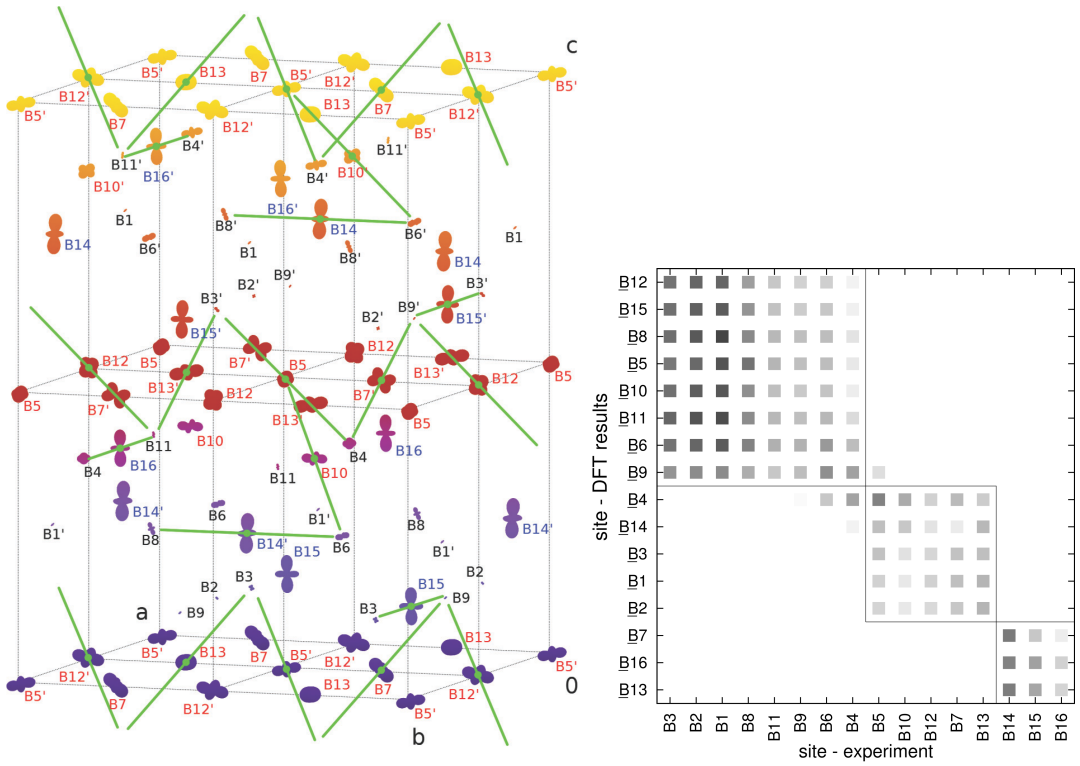

Figure 3.6: Left: graphically represented anisotropy of calculated hyperfine magnetic fields of octahedral Fe sites in the magnetite Cc unit cell. Green lines denote the trimeron structures, where central Fe^{2+}-like atoms display increased anisotropy, compared to relatively isotropic Fe^{3+}-like atoms situated at the end of trimerons. Right: assignment of the ^{57}Fe NMR spectral lines to octahedral Fe sites. Intensity of the squares corresponds to mean square deviation between the DFT and NMR results. Adopted from Ref. [VC9].

right), which allowed to determine the $\gamma \sim 0.62$ from ^{57}Fe, in a good agreement with the value from ^{67}Zn NMR results. Our approach thus also demonstrated that NMR is suitable tool to study the atomic arrangement, even in such relatively disordered systems.

3.2 Magnetite and other ferrites

The concept of combining experimental local probe (such as NMR) with electronic structure calculations has been successfully applied – besides the hexaferrites – also to various other magnetic iron oxides. In this section the papers concerning structure of magnetite are presented, followed by presentation of two works where electric quadrupole interaction played a significant role in the analysis of NMR spectra of ferrites for isotopes other than ^{57}Fe.

Low temperature phase of magnetite

One of the most intricate iron oxide structures is that of magnetite which occurs below the Verwey phase transition $T_V \sim 120$ K [71]. The complications with studying such structure are due to large size of the monoclinic unit cell with 8

unique tetrahedral and 16 octahedral Fe positions, while in addition the structure differs only very slightly from the high temperature cubic structure – by monoclinic angle $\sim$ 90.24 degrees and orthorhombic deformation of about 0.3 % [72]. But more importantly, the peculiarity of magnetite at low temperature arises from the rich possibilities of charge and orbital order, allowed by the fact that magnetite is a mixed valence compound: in the cubic phase the octahedral Fe are all equivalent, whereas in the low temperature phase a delicate and unique charge and orbital structure of octahedral Fe is established. Consequently, the charge and orbital ordering, the value of T_V and the presence of the Verwey transition (or lack of it) is very sensitive to exact stoichiometry [73] and the number of defects [74], even the history of the particular magnetite sample can be important [75, 76].

Current understanding is that below T_V the octahedral Fe atoms form a network of linear objects, nicknamed "trimerons", each consisting of three neighboring Fe atoms. In a trimeron the central Fe donates part of its minority-spin electron density to the remaining two atoms, which in turn are slightly shifted toward the center [77].

From the point of view of NMR, the situation with magnetite is quite ironic: ^{57}Fe NMR is the only spectroscopy that can resolve all the 24 nonequivalent Fe sites, and thus during the history of magnetite research the method significantly contributed to determination of the Cc structure [78], yet the full assignment of the individual spectral lines is not available to this day. In Ref. [VC9] we attempted to tackle this problem by utilizing both presented approaches [VC1, VC2] for comparison of hyperfine fields obtained by NMR and DFT, i.e., DFT calculations were employed to obtain the hyperfine fields including their anisotropic parts for all Fe sites (see Fig. 3.6 left panel). These results were then compared with available NMR experiments, which were the sophisticated measurements of ^{57}Fe NMR dependences on direction of external magnetic field by Moriji Mizoguchi [79]. In order to allow the comparison, the direction of the magnetization was calculated (using the magnetic anisotropy of magnetite [80]) for a given direction of applied external magnetic field in the experiment. Then the anisotropy tensors for all 16 octahedral Fe sites were obtained by fitting the experimental dependences.

The DFT calculations were designed to mimic the experiment and analogous set of anisotropy tensor was derived from the calculated hyperfine fields. By minimizing the mean square deviation of the calculated and experimental fields (or NMR frequencies) we were able to correlate the NMR and DFT data. Although making most of the method (using both the zero-field frequencies and the anisotropic contributions responsible for the angular dependences), our approach yielded only a partial assignment: the 16 octahedral Fe sites in the unit cell can be sorted into three groups 8:5:3, however, inside these groups, as well as inside the group of 8 tetrahedral sites, the lines cannot be identified any further (Fig. 3.6 right panel). The values of spectroscopic parameters within each of the groups are unfortunately too similar to allow for further refinement. These results supported the idea of trimeron structure against other proposed arrangements, e.g., [72, 81]. We proved that character of the ^{57}Fe NMR spectrum, particularly the segregation into 8:5:3, and the trimeron structure are mutually compatible, and it is a topic for future studies, whether this relationship is exclusive.

Another approach of tackling the low temperature phase was undertaken in Ref. [VC10], this time, however, for the Mössbauer spectroscopy, which is a frequent

experimental method for studying magnetite and other iron oxides. Although this method lacks the high resolution in hyperfine magnetic fields compared to NMR, for ^{57}Fe isotope Mössbauer makes up for it by availability of two extra spectroscopic quantities: the quadrupole interaction and the isomer shift. As already mentioned, the quadrupole interaction is not present in NMR for ^{57}Fe isotope with spin $1/2$, but appears in Mössbauer spectroscopy due to spin value of the excited nuclear state of ^{57}Fe being $3/2$. Similarly, the isomer shift is observable thanks to the difference in nuclear radii of excited and ground state of the ^{57}Fe nucleus.

Unlike ^{57}Fe NMR, where generally each non-equivalent Fe site contributes by a single line, in Mössbauer spectroscopy the higher number of possible nuclear transitions between excited and ground state of ^{57}Fe induces up to eight, but typically six spectral lines per Fe site in magnetic materials. Detailed and reliable analysis of Mössbauer spectra with higher number of non-equivalent sites then becomes a difficult procedure of resolving numerous overlapping sextets. To describe the experiment, one then has to adopt a strategy of decomposing to lower number of sextets, usually using some phenomenological assumptions.

Since the overall analysis is limited by such assumptions, which makes a comparison of different Mössbauer studies complicated, we aimed to propose a universal decomposition to four sextets [VC10]. Utilizing our experience with such grouping for the lines in ^{57}Fe NMR spectrum, we suggested decomposing the Mössbauer spectrum of low-temperature magnetite phase into one sextet for tetrahedral Fe and three sextets (with intensities 8:5:3) for the octahedral Fe. To demonstrate that such approximation is adequate, the complete set of parameters for the four sextets was calculated by DFT, i.e., the hyperfine magnetic field, the electric field gradient, and the isomer shift. Then, the Mössbauer spectrum of high-quality single crystal of magnetite was acquired and the approximation by four sextets applied to fit the measured spectrum – successfully, as no feature of the experimental Mössbauer spectrum was left unexplained by the model. We thus proposed a simple tool for analysis of Mössbauer experiments not only in physics, but also in other fields such as chemistry or geology, where often the goal is to determine the changes of magnetite amount in a measured sample or even only check for its presence.

High temperature phase of magnetite

The low temperature phase is both interesting and challenging for its complex crystallographic and domain structure, orbital and charge ordering, and many related physical properties or phenomena, such as the nature of the Verwey transition itself, axis switching induced by external magnetic field [82, 83], or anisotropy [80]. In contrast to these features, the high temperature cubic phase appears to be rather dull. However, recent experiments [84–86] reveal high temperature magnetite phase as a rather dynamic state, especially in the vicinity of the Verwey transition where some form of short-range order resembles ordering of the low-temperature phase.

Besides, there is another interesting magnetic property of magnetite: the behavior of its magnetocrystalline anisotropy and especially the reorientation transition at temperature $T_{\mathrm{SR}} \sim 130$ K, which has long time been disputed to be connected with the Verwey transition [87–89]. The reorientation transition is well visible in the ^{57}Fe NMR experiments: for direction of magnetization along $\langle 100 \rangle$ direction

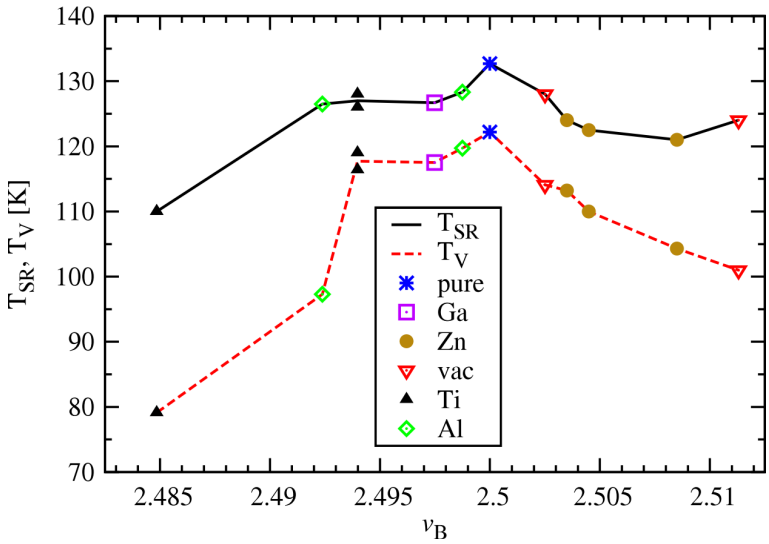

Figure 3.7: Spin reorientation temperature T_{SR} and Verwey transition temperature T_V in dependence on the average valency ν_B of octahedral Fe atoms. Adopted from Ref. [VC11].

(below T_{SR}) all ^{57}Fe nuclei in octahedral Fe sites resonate in a single spectral line, while above T_{SR} with magnetization direction $\langle 111 \rangle$ the line splits 1:3 due to anisotropy of hyperfine interaction.

Studying the influence of Ti, Zn, Al, and Ga doping or low amount of vacancies small on the Verwey transition and the spin reorientation transition [VC11] by means of ^{57}Fe NMR and ac susceptibility measurements, we found a correlation between their temperatures, T_{SR} and T_V (Fig. 3.7). The study was accompanied by calculations of electronic structure to evaluate the valence states in pure and substituted magnetites. Using the calculated valence we showed that the charge density due to defect/substitution spreads over a large distance, and thus the magnetocrystalline anisotropy is not induced by localized anisotropic ions. As a consequence, T_{SR} is only slightly modified by the charged defects.

Additionally, the anisotropy constants in pure cubic magnetite were calculated and confronted with experiments [80] and thermodynamic models [88], which allowed us to propose the following explanation of the anomalous temperature dependence of the magnetocrystalline anisotropy in the cubic phase of magnetite. At temperatures above T_V magnetite displays small magnetocrystalline anisotropy with K_1 anisotropy constant negative. Excited state is degenerate, with large anisotropy and positive K_1. The gap between this excited state and the ground-state is sensitive to temperature: it is wide at high temperatures but closes with decreasing temperature and eventually, at T_{SR}, leads to change of sign of K_1 constant, and further at T_V the degeneracy of the excited state is lifted entirely and its contribution to K_1 disappears.

Magnetic systems with electric quadrupole interaction

As was shown for the ^{57}Fe isotope, the structural information stemming from the quadrupole interaction can be extracted by the Mössbauer spectroscopy but not by NMR (spin $1/2$ in the ground state of ^{57}Fe), nevertheless, this is not the case for

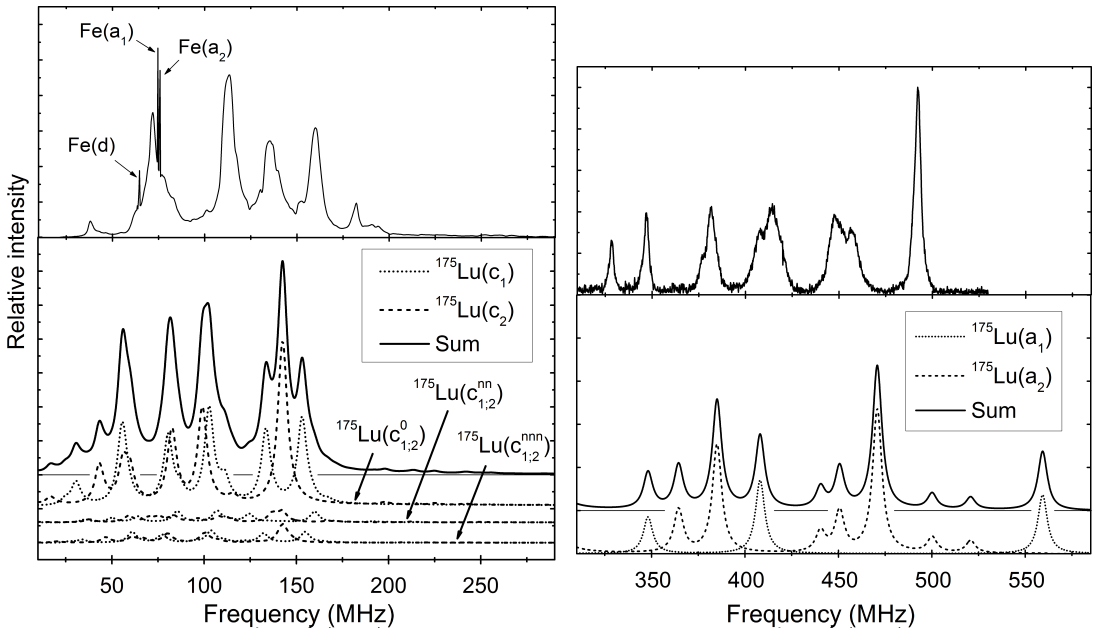

Figure 3.8: Comparison of experimental ^{175}Lu NMR spectrum and the one simulated from *ab initio* calculated EFG and hyperfine fields in lutetium iron garnet. Left panel: contributions from lutetium atoms neighboring to antisite Lu(a) defect, or being next-nearest neighbors, as well as more distant Lu atoms are denoted with indices nn, nnn, and 0. Right panel: contribution directly from ^{175}Lu forming the Lu(a) defect. Adopted from Ref. [VC12].

many other isotopes with higher spins, which are available to NMR spectroscopy. Then, in presence of electric quadrupole interaction, the calculation of electric field gradients is the key part to understand, assign, or even predict the experimental NMR spectra, as will be shown in the remaining presented papers.

In lutetium iron garnet (LuIG) the NMR spectrum consists, besides the ^{57}Fe isotope resonance, also from intensive and exceptionally broad lines of ^{175}Lu isotope (spin $^7/_2$). The combination of strong electric quadrupole interaction and non-zero transferred hyperfine magnetic field on ^{175}Lu yields a general case where none of the ^{175}Lu nuclear transitions can be considered as "forbidden" and thus up to 28 lines for each of the two (magnetically) non-equivalent Lu sites can be expected. The measured NMR spectrum reflects such scenario and contains a pile of overlapping resonance lines in a broad range of about 20–300 MHz. Additionally, there is another, weaker resonance detectable at higher frequencies, about 300–550 MHz. The lower frequency spectrum must clearly originate from the ^{175}Lu in the dodecahedral sites, nominal for lutetium atoms. This was confirmed by the calculations of LuIG electronic structure [VC12], where simulated ^{175}Lu NMR spectrum from the calculated parameters matched well with the experiment at low frequencies (Fig. 3.8 left panel).

Different situation, however, occurs for the weaker resonance at higher frequencies where two equivalent explanations can be proposed. First, lutetium has another, less abundant stable isotope ^{176}Lu with spin 7 and slightly higher nuclear moments μ and Q compared to ^{175}Lu, and so the resonance at higher frequencies could correspond to ^{176}Lu in dodecahedral sites. Or second, the garnet contains small amount of anti-site defect, consisting of a Lu atom entering an octahedral

site which nominally belongs to Fe, and thus the resonance of ^{175}Lu in such octahedral sites could alternatively give rise to the spectrum at higher frequencies. Both scenarios would produce quite similar intensity of the higher frequency spectrum, about 50 times lower than the intensity of the main ^{175}Lu NMR spectrum at low frequencies, because the abundance of ^{176}Lu is 2.6 % and the concentration of anti-site defect is ~ 1 %, as can be determined from ^{57}Fe spectra.

The issue was resolved by calculating the hyperfine parameters for both scenarios [VC12], i.e., the hyperfine fields as well as electric field gradients at lutetium nuclei were to be obtained. Unlike in case ^{57}Fe where a correction to calculated magnetic fields is required, for lutetium the situation is more favorable and no correction needs to be developed. This is because lutetium atom in the garnet does not possess any appreciable magnetic moment, therefore, the problematic core contribution to the contact hyperfine magnetic field is not encountered at all. The contact field on Lu nucleus is produced predominately due to transferred field from neighboring Fe atoms, via oxygen ligands and valence Lu 6s electrons. In such cases, the calculated fields do not suffer from systematic underestimation [20, 22]. Likewise, the calculated electric field gradients are usually in a good agreement with the experiments [90, 91].

Hyperfine parameters calculated for the ^{175}Lu occupying octahedral sites yielded NMR spectrum well corresponding to the experimentally observed weaker resonance at higher frequencies (Fig. 3.8 right panel). Our calculations thus explained the observed frequency shift for the octahedral (anti-site) Lu resonance, which is caused by a considerable transferred magnetic field ~ 21.7 T, about 4 times larger than the values 5.9 and 3.9 T for dodecahedral Lu (the nominal Lu sites). Presence of such increased transferred field is understandable, as the anti-site Lu, being located within the magnetic Fe sublattice, is exposed to stronger exchange interactions in comparison to the dodecahedral sites. The alternative scenario with ^{176}Lu in dodecahedral sites yielded resonance lines in a similar range as dodecahedral ^{175}Lu, i.e., in a broad range of frequencies below 150 MHz, and thus ^{176}Lu resonance is most probably overlapped by much more intensive ^{175}Lu spectrum. Therefore this alternative could be rejected.

Another example concerning the electric quadrupole interaction and determination of EFG parameters was NMR, Mössbauer, and DFT study of ilmenite $FeTiO_3$ [VC13]. The local structure of titanium was investigated at various temperatures by ^{47,49}Ti NMR in magnetic field 9.4 T and analogously for ^{57}Fe by Mössbauer spectroscopy in zero field. Both experimental methods were then compared via the spectroscopic parameters to the results of calculations of electronic structure. The ilmenite structure is relatively simple, since nominally the Fe and Ti cations occupy one octahedral site each, however, the NMR spectroscopy of titanium brings issues on its own. The two stable titanium isotopes, ^{47}Ti and ^{49}Ti, have unusually close values of gyromagnetic ratios, and both also possess considerable electric quadrupole moments, which leads to an unavoidable overlap of the their NMR spectra.

Ilmenite is paramagnetic at room temperature and its titanium NMR spectrum is relatively well resolved, allowing to extract the EFG parameters directly by fitting the whole powder-pattern of the quadrupole spectrum including satellite transitions. EFG parameters, $V_{zz} = 2.58(4) \times 10^{21}$ Vm^{-2}, $\eta = 0.029(3)$, obtained in such way are much more trustworthy, compared to more usual procedure when only

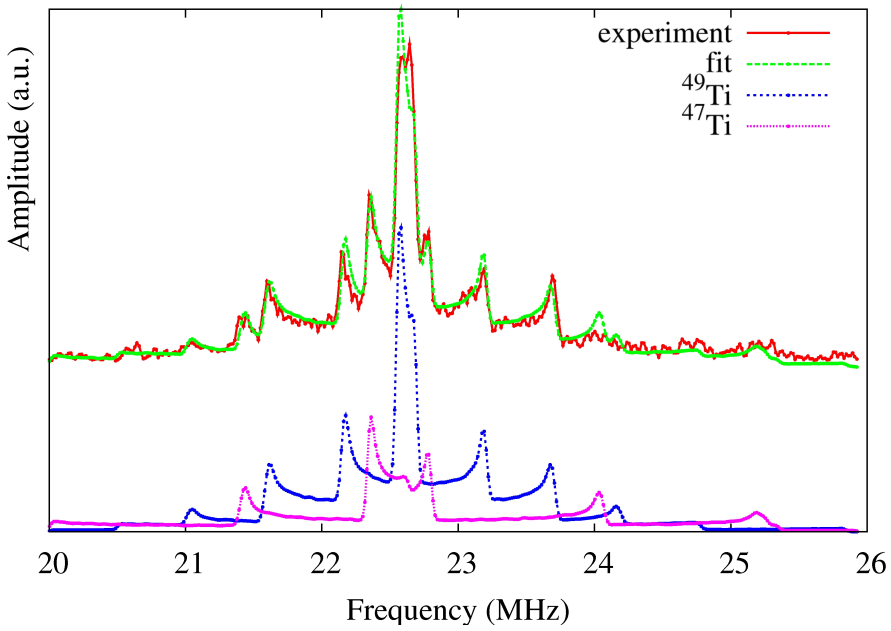

Figure 3.9: ^{47}Ti and ^{49}Ti NMR spectrum of $FeTiO_3$ at 300 K, fitted and decomposed to contributions of titanium isotopes. Adopted from Ref. [VC13].

the central transition is measured and analyzed [92] and yields $V_{zz} = 2.1(2) \times 10^{21}$ Vm^{-2}, and higher value of $\eta = 0.35(10)$. For ^{57}Fe the parameter $V_{zz} = 8.6(2) \times 10^{21}$ Vm^{-2} was acquired by the Mössbauer experiment at 5 K. Our DFT calculations of electronic structure provided EFG values in a relatively good agreement with both spectroscopic methods, $V_{zz} = 2.24(10)$ for Ti and $V_{zz} = 6.95(10) \times 10^{21}$ Vm^{-2} for Fe. The parameter η was zero due to symmetry constraints – presence of 3-fold symmetry axis of Fe and Ti sites.

In further analysis we broke the local symmetry of Ti sites in order to study a possible deviation from the trigonal symmetry and to estimate its influence on EFG parameters. Optimizing the structure with lowered symmetry yielded $\eta \sim 0.17(5)$ in the calculations, which corresponds to the small non-zero value of asymmetry η being indeed found in the ^{47,49}Ti NMR experiments. However, such slight deviation of η from zero could also be interpreted as an effect of distribution of EFG around some mean value, e.g., due to defects or other perturbations of the structure.

3.3 Non-magnetic systems

In contrast to magnetically ordered materials where large values of hyperfine magnetic field can give rise to measurable NMR even without application of external magnetic field, in a non-magnetic system the contributions to hyperfine magnetic field for electrons with opposing spins effectively cancel out. As a consequence, the time-averaged mean value is zero and the main part of the magnetic field is usually supplied by a well-defined homogeneous external field. The spectroscopic information – analogous to hyperfine fields – is then contained in the chemical or Knight shifts. The approach of comparing NMR experiments with DFT calculations can

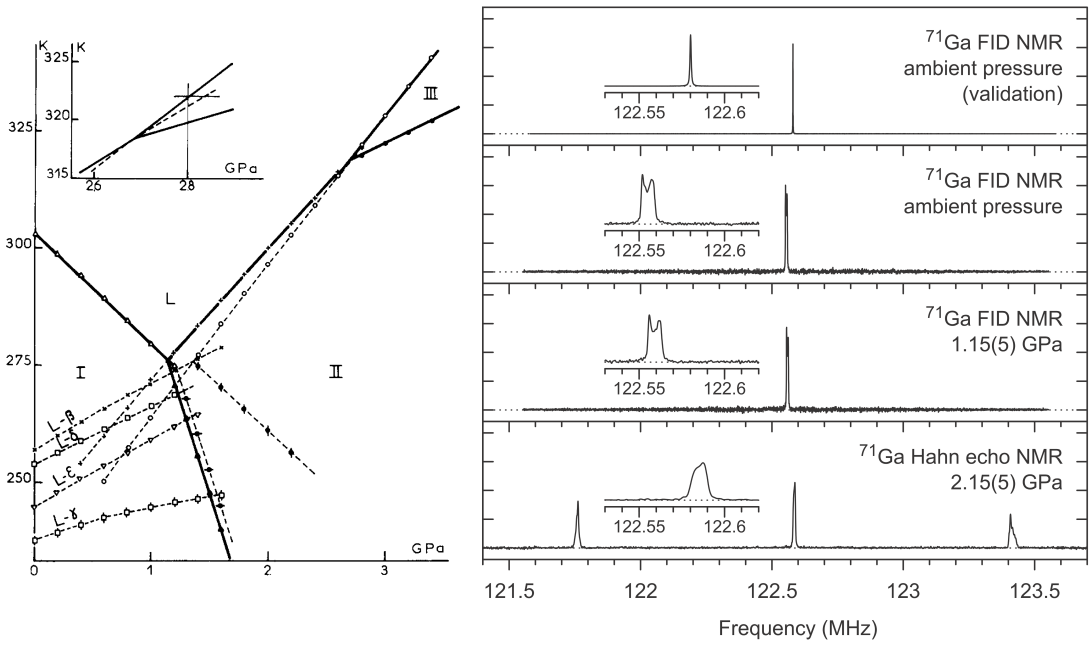

Figure 3.10: Equilibrium phase diagram of gallium, depicting the triple point as well as several metastable equilibrium phase boundaries, taken from [93]. Example of ^{71}Ga NMR spectra of gallium at room temperature for several different pressures, taken from [VC14].

thus be used in the same way, since both shifts can be reasonably calculated, and of course the electric quadrupole interaction is again considered if present in the studied system. In the following text we present four such works where the NMR-DFT comparison was successfully applied in studying non-magnetic solid-state systems.

Local structure of metals

Unlike most of other pure elements, which tend to crystallize as high-symmetry structures under ambient conditions, elemental gallium forms a rather complex structure with orthorhombic unit cell. Gallium displays a rich polymorphism [93–95] and besides the Ga-I phase (orthorhombic, also denoted as α-Ga) or Ga-II (bcc) the phase diagram contains a plethora of stable and metastable crystal phases (Fig. 3.10). Moreover, the liquid phase as well as several solid phases may be significantly supercooled [96], and thus the structure of gallium at a given temperature and pressure depends also on how this state was reached. The NMR spectroscopy has been successfully applied for studying the liquid [97, 98] as well as some of the most common solid phases of gallium [99–101]. The phases emerging above the liquid–Ga-I–Ga-II triple point that require higher pressure have rarely been measured by NMR [102] though, and thus we studied the structure of gallium metal under pressure up to 2.2 GPa by means of ^{71}Ga NMR in combination with DFT calculations [VC14].

At room temperature and ambient pressure the gallium was liquid at room temperature, but under applied pressure of ~ 2 GPa transformed into a crystal phase as manifested by quadrupole splitting in the ^{71}Ga NMR spectrum (Fig. 3.10). The isotope ^{71}Ga has nuclear spin 3/2 and so the electric quadrupole splitting

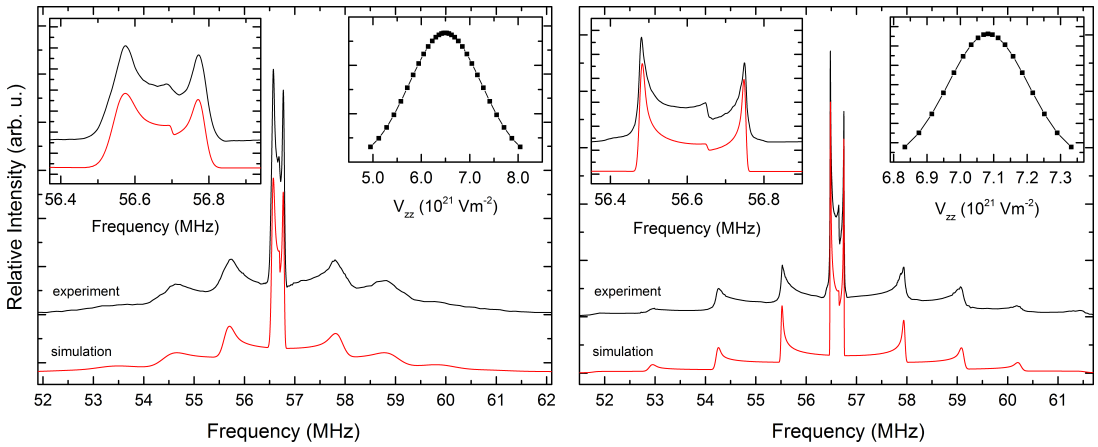

Figure 3.11: ^{139}La NMR spectra of $LaCuAl_3$ (left) and $LaAuAl_3$ (right) with their simulations using distribution of V_{zz} parameter. Adopted from Ref. [VC15].

can be expected if the local symmetry of gallium site differs from cubic. Indeed, the experimentally observed spectrum was quadrupolarly split and corresponded to a single crystal site with axial symmetry ($\eta = 0$) and $V_{zz} \sim 1.58 \times 10^{21}$ Vm^{-2}.

For room temperature and pressure 2.2 GPa, several crystal structures of gallium can be expected: cubic Ga-II, tetragonal Ga-III, and monoclinic β-Ga phase. However, for each of these three structures all Ga atoms in the unit cell are equivalent, hence any of these three phases could give rise to the observed spectrum. Therefore, in order to attribute the ^{71}Ga NMR spectrum to one particular structure, we confronted the experimental EFG parameters with those obtained from calculations of electronic structure.

Since the electric field gradients are readily available in the WIEN2k calculations in each SCF iteration, the only missing aspect in the DFT model was the applied pressure. Pressure dependences were obtained by changing the unit cell volume, while maintaining equilibrium, i.e., the remaining structural degrees of freedom (ratios of lattice parameter and internal atomic positions) were properly optimized. The value of pressure corresponding to a given volume was then extracted from fit to Birch-Murnaghan equation of state [103]. This process allowed direct comparison of the calculated EFG parameters with those derived from the experiment at 2.15 GPa. Our calculations yielded $V_{zz} = 1.64 \times 10^{21}$ Vm^{-2} and $V_{zz} = -0.96 \times 10^{21}$ Vm^{-2} for Ga-III and Ga-II (both with $\eta = 0$), and $V_{zz} = 2.67 \times 10^{21}$ Vm^{-2}, $\eta = 0.37$ for β-Ga phase. The obvious assignment of the phase observed in experiment to Ga-III was further supported by calculation of Knight shift $K = 0.45$ %, which also matched well with the value in experiment $K = 0.47$ %, whereas the calculated K for Ga-II and β-Ga phase was $K = 0.42$ % and $K = 0.49$ %, respectively. Such agreement of NMR parameters lead us to interpret unambiguously the experimental ^{71}Ga NMR spectrum as the tetragonal Ga-III phase.

Another non-magnetic metallic system where investigation of the crystal structure was addressed by NMR spectroscopy and DFT calculations was $LaCuAl_3$ [VC15]. Our aim was to show whether the local environment of lanthanum in $LaCuAl_3$ is uniform or rather there are more non-equivalent La sites due to Cu/Al disorder, as this information was essential for understanding the structure of the

compound's phonon-analogue $CeCuAl_3$. Inelastic neutron scattering experiments [104] revealed that the neutron energy spectra of the cerium compound contain an extra peak in addition to the two peaks expected from crystal electric field theory. In order to interpret such results the magnetoelastic interaction between the crystal electric field excitations and the lattice vibrations (so called "vibron") had to be incorporated. On the other hand, alternative explanation could consist simply in presence of multiple non-equivalent Ce sites with different crystal field parameters. NMR spectroscopy was chosen as a suitable method to resolve whether such scenario is possible. Because cerium lacks suitable NMR isotope, only an indirect investigation via NMR of Al and Cu nuclei would be possible. Therefore the study was performed with phonon-analogue compound containing La instead of Ce. This brings additional benefit, as the La compounds are nonmagnetic and thus not affected (broadened) by hyperfine magnetic fields.

A comparative approach was undertaken with $LaCuAl_3$, as a compound presumably having more than one La site, and $LaAuAl_3$, as a compound known to be well ordered, i.e., having a single type of La surroundings. The NMR spectra of ^{139}La, ^{27}Al, and ^{65}Cu were recorded for $LaCuAl_3$ in 9.4 T at room temperature, and all displayed well visible features of electric quadrupole interaction. When confronted with results on the ordered $LaAuAl_3$ system, the ^{139}La spectra of $LaCuAl_3$ were significantly more broadened in comparison with those of $LaAuAl_3$ (see Fig. 3.11).

In order to determine the source of such broadening, DFT models of $LaCuAl_3$ and $LaAuAl_3$ with various cationic configurations and stoichiometries were calculated and for each such model the EFG parameters were evaluated. The ^{139}La spectrum in $LaAuAl_3$ could be interpreted by a single spectral component and corresponded well to the (ordered) $I4mm$ structure, and at the same time, the EFG parameters calculated for other possible Au/Al arrangements were significantly different and could not contribute to the spectrum. Whereas in case of $LaCuAl_3$ the ^{139}La spectra displayed a wide distribution of spectral parameters, which could not be explained by a single La environment – at least one additional structure with different Cu/Al arrangement was needed to interpret the observed spectra. Similar observations were made for ^{27}Al NMR spectra, and in case of $LaCuAl_3$ also for ^{65}Cu NMR spectrum. Therefore, we concluded that multiple non-equivalent La positions must be present in the crystal structure of $LaCuAl_3$. This finding was further elaborated and justified by analysis of calculated configurational energies, where we showed that $LaCuAl_3$ has a stronger tendency to atomic Cu/Al mixing compared to Au/Al case in $LaAuAl_3$.

EFG and band-inversion in topological insulator

The ^{209}Bi NMR accompanied by DFT calculations was used to study Bi_2Se_3 topological insulator [VC16], which is a system where spin-orbit interaction makes the electronic states in bulk different from those near the surface. Strong spin-orbit coupling in the bulk Bi_2Se_3 induces so called "band inversion", i.e., the position of Bi p_z states in energy is decreased and the energy of Se p_z states increased. This leads to charge transfer from Se to Bi and such transfer is manifested as relatively small quadrupole splitting observed in ^{209}Bi NMR spectrum. The splitting further decreases with increasing concentration of charge carriers.

The corresponding ^{209}Bi EFG parameters were obtained from DFT calculations

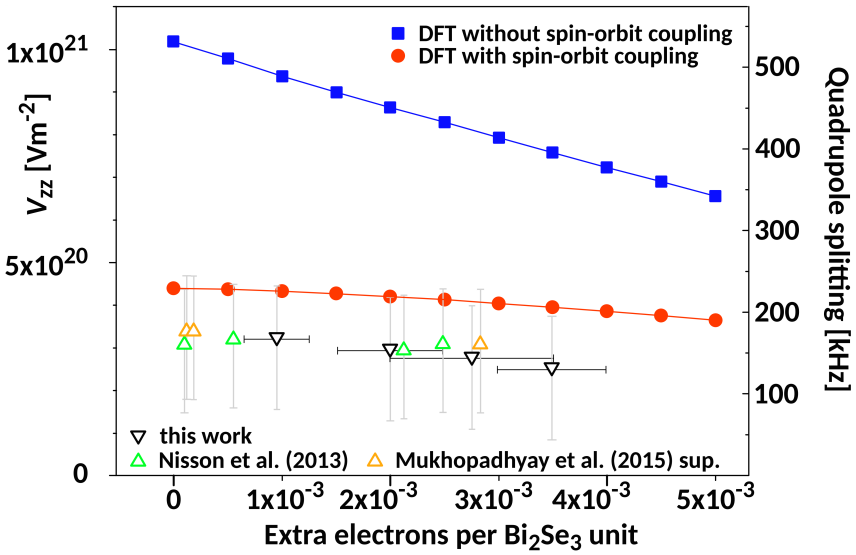

Figure 3.12: Calculated V_{zz} with (red) and without (blue) spin-orbit coupling in dependence on the carrier concentration are compared with experimental quadrupole splittings measured in Ref. [VC16] (black triangles), [105] (green triangles), and [106] (orange triangles). Horizontal error bars indicate the expected variation of the carrier concentration among the samples, vertical error bars indicate the variation of V_{zz} due to uncertainty of ^{209}Bi quadrupole momentum. Adopted from Ref. [VC16].

of Bi_2Se_3 with extra charge added into the unit cell in order to model realistic carrier concentrations (see Fig. 3.12). We showed that the EFG on Bi appears due to anisotropy of its $6p$ states: $6p_z$ states are less occupied than the $6p_x$ and $6p_y$ states. And since the extra charge enters the $6p_z$ states predominantly, the increase of carrier concentration reduces the EFG on ^{209}Bi.

When the spin-orbit interaction is enabled in the calculation, band inversion occurs, which is accompanied by additional transfer of electronic density from Se to Bi p states. The calculations thus allowed us to explain the abrupt decrease of the EFG on bismuth when the strong spin-orbit interaction is present.

Investigation of cationic preference

Not only interpretation of NMR spectra but an additional insight was brought by employing the DFT calculations of $Lu_3Al_{5-x}Ga_xO_{12}$ garnets [VC17], where the atomic arrangement of Al and Ga was studied. The occupation of tetrahedral and octahedral positions of the garnet lattice by Al and Ga atoms – important for scintillating properties of the material [107] – was independently determined from spectral intensities of ^{27}Al and ^{71}Ga NMR. The NMR results were then confronted with appropriate DFT models and both methods indicated a strong preference of Ga to occupy tetrahedral sites, regardless of Ga concentration x.

Such result appears as a paradox, since gallium has larger ionic radius than aluminium and the tetrahedron in the garnet structure has significantly smaller volume than the octahedron. Besides, there is no apparent difference in the electronic structure, since both Al an Ga atoms possess ns^2np^1 valence electrons that

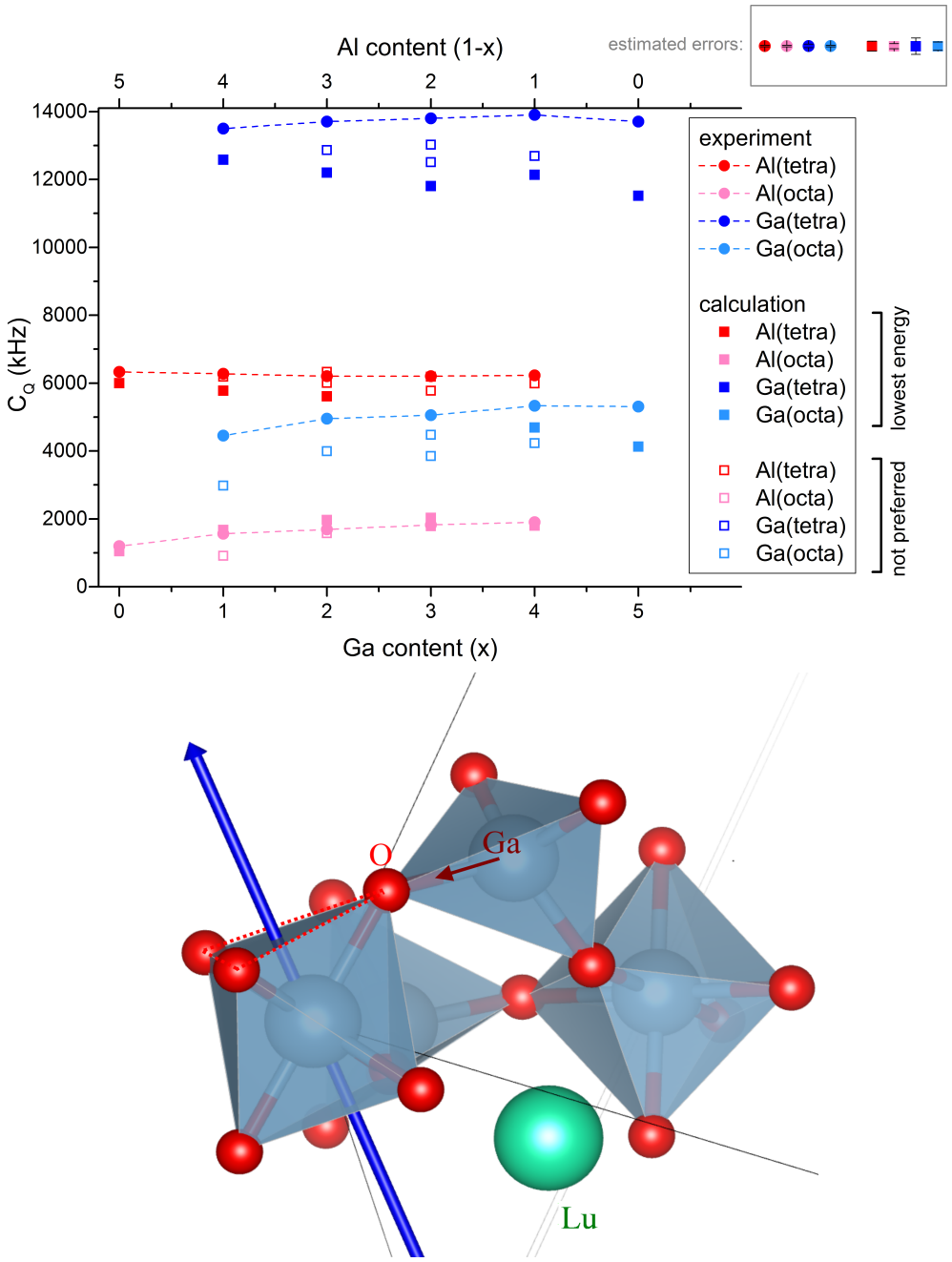

Figure 3.13: Top: Aluminium and gallium quadrupole constants as determined from NMR experiments and from DFT calculations for the mixed $Lu_3Al_{5-x}Ga_xO_{12}$ garnets. Bottom: Local structure of the garnet with indicated changes upon Ga substitution. Inflation of Ga tetrahedron further increases the trigonal distortion of the oxygen octahedron, while the tetrahedron is rotated to accommodate the shift of the shared oxygen. Partially adopted from Ref. [VC17].

favor the formation of hybridized sp^3 orbitals in the oxygen tetrahedron. However, from our DFT calculations we were able to show that, despite being fully occupied, the semi-core Ga $3d$ electrons are slightly involved in the interactions, and thus become the essential factor making Ga less compatible for octahedral environment. Together with higher electronegativity of Ga, this explained the observed tendencies of atomic distribution in the garnet structure.

Besides the atomic arrangement, the quadrupole coupling constants and chemical shift parameters for Al and Ga nuclei were calculated in a good agreement with the NMR experiments. This allowed us to understand why for octahedral Al and Ga the measured EFG parameters increase with increasing Ga content, while the tetrahedral EFGs keep constant. The DFT modelling showed that the structural relaxation after substitution of Al by larger Ga proceeds via deformation of the octahedrons while the tetrahedrons are rotated in the process, but otherwise left relatively intact.

Concluding remarks

The presented thesis described – as a common theme – the connection of two methods for studying solids: nuclear magnetic resonance experiments and density functional theory calculations. These methods were briefly introduced in the first chapters, and then their mutually beneficial combination was demonstrated in a set of papers concerning magnetic, but also several non-magnetic solid-state systems. The original pathway of this interaction – lying in calculations providing help with the interpretation of experiments – became more and more often completed with the support flowing in the opposite direction, as the precise experiments provided an anchor to reality for the calculations. We tried to show both the difficulties and the advantages of such approach and the deeper understanding it provides.

There are many directions for future developments of this combined method, mostly consisting of improvements on the side of calculations. For example in magnetic materials, the electronic correlations should be better addressed by utilizing beyond-DFT methods. Nowadays, such solution has become feasible in form of incorporating many-body methods (e.g., dynamical mean field theory) selectively within the DFT framework. For nonmagnetic materials, potentials for considering dispersion forces have been recently developed and implemented in all-electron DFT methods, which allows better descriptions of systems we would like to study, such as crystals containing water molecules with hydrogen bonds or layered structures with inter-layer van der Waals forces.

References

[1] C. P. Slichter, *Principles of magnetic resonance*, Vol. 1 (Springer-Verlag, Berlin Heidelberg, 1990).

[2] A. Abragam, *The principles of nuclear magnetism* (Clarendon Press, Oxford, 1961).

[3] E. A. Turov and M. P. Petrov, *Nuclear magnetic resonance in ferro- and antiferromagnets* (Halsted Press, New York, 1972).

[4] P. Hohenberg and W. Kohn, Phys. Rev. **136**, B864–B871 (1964).

[5] W. Kohn and L. J. Sham, Phys. Rev. **140**, A1133–A1138 (1965).

[6] J. P. Perdew, K. Burke, and M. Ernzerhof, Phys. Rev. Lett. **77**, 3865–3868 (1996).

[7] J. P. Perdew and A. Zunger, Phys. Rev. B **23**, 5048–5079 (1981).

[8] J. P. Perdew, J. A. Chevary, S. H. Vosko, K. A. Jackson, M. R. Pederson, D. J. Singh, and C. Fiolhais, Phys. Rev. B **46**, 6671–6687 (1992).

[9] E. Wimmer, H. Krakauer, M. Weinert, and A. J. Freeman, Phys. Rev. B **24**, 864–875 (1981).

[10] M. Weinert, E. Wimmer, and A. J. Freeman, Phys. Rev. B **26**, 4571–4578 (1982).

[11] D. R. Hamann, M. Schlüter, and C. Chiang, Phys. Rev. Lett. **43**, 1494–1497 (1979).

[12] D. Vanderbilt, Phys. Rev. B **41**, 7892–7895 (1990).

[13] O. K. Andersen, Phys. Rev. B **12**, 3060–3083 (1975).

[14] P. Blaha, K. Schwarz, F. Tran, R. Laskowski, G. K. H. Madsen, and L. D. Marks, "WIEN2k: An APW+lo program for calculating the properties of solids", J. Chem. Phys. **152**, 074101 (2020).

[15] E. Sjöstedt, L. Nordström, and D. J. Singh, Solid State Commun. **114**, 15–20 (2000).

[16] D. Singh, Phys. Rev. B **43**, 6388–6392 (1991).

[17] D. Singh, Phys. Rev. B **40**, 5428–5431 (1989).

[18] R. Yu, D. Singh, and H. Krakauer, Phys. Rev. B **43**, 6411–6422 (1991).

[19] S. Blügel, H. Akai, R. Zeller, and P. H. Dederichs, Phys. Rev. B **35**, 3271 (1986).

[20] H. Katayama, K. Terakura, and J. Kanamori, Solid State Commun. **29**, 431–434 (1979).

[21] M. S. R. Laskar, S. Saha, R. Palit, S. N. Mishra, F. S. Babra, S. Biswas, P. Singh, and S. K. Mohanta, Hyperfine Interact. **240**, 96 (2019).

[22] S. Cottenier and H. Haas, Phys. Rev. B **62**, 461–467 (2000).

[23] A. de Oliveira, M. V. Tovar Costa, N. A. de Oliveira, and A. Troper, J. Magn. Magn. Mater. **320**, e446–e449 (2008).

[24] M. Filatov, Coord. Chem. Rev. **253**, 594–605 (2009).

[25] H. Ebert, P. Strange, and B. L. Gyorffy, J. Phys. F **18**, L135–L139 (1988).

[26] P. Novák, J. Kuneš, W. E. Pickett, W. Ku, and F. R. Wagner, Phys. Rev. B **67**, 140403 (2003).

[27] E. N. Kaufmann and R. J. Vianden, Rev. Mod. Phys. **51**, 161–214 (1979).

[28] K. Schwarz and P. Blaha, Z. Naturforsch. **47**, 197–202 (1992).

[29] A. R. Edmonds, *Angular momentum in quantum mechanics* (Princeton University Press, Princeton NJ, 1974).

[30] F. Haarmann, K. Koch, D. Grüner, W. Schnelle, O. Pecher, R. Cardoso-Gil, H. Borrmann, H. Rosner, and Y. Grin, Chem. Eur. J. **15**, 1673–1684 (2009).

[31] F. Haarmann, K. Koch, P. Jeglič, O. Pecher, H. Rosner, and Y. Grin, Chem. Eur. J. **17**, 7560–7568 (2011).

[32] W. Lipscomb, "The chemical shift and other second-order magnetic and electric properties of small molecules", Adv. Magn. Opt. Reson. **2**, 137–176 (1966).

[33] R. Ditchfield, Mol. Phys. **27**, 789–807 (1974).

[34] P. E. Blöchl, Phys. Rev. B **50**, 17953–17979 (1994).

[35] C. J. Pickard and F. Mauri, Phys. Rev. B **63**, 245101 (2001).

[36] J. R. Yates, C. J. Pickard, and F. Mauri, Phys. Rev. B **76**, 024401 (2007).

[37] R. Laskowski and P. Blaha, Phys. Rev. B **85**, 035132 (2012).

[38] R. Laskowski and P. Blaha, Phys. Rev. B **85**, 245117 (2012).

[39] R. Laskowski and P. Blaha, Phys. Rev. B **89**, 014402 (2014).

[40] F. Blanc, J.-M. Basset, C. Copéret, A. Sinha, Z. J. Tonzetich, R. R. Schrock, X. Solans-Monfort, E. Clot, O. Eisenstein, A. Lesage, and L. Emsley, J. Am. Chem. Soc. **130**, 5886–5900 (2008).

[41] T. Charpentier, S. Ispas, M. Profeta, F. Mauri, and C. J. Pickard, J. Phys. Chem. B **108**, 4147–4161 (2004).

[42] R. K. Harris, S. A. Joyce, C. J. Pickard, S. Cadars, and L. Emsley, Phys. Chem. Chem. Phys. **8**, 137–143 (2006).

[43] V. D. Doroshev, V. A. Klochan, N. M. Kovtun, and V. N. Seleznev, Phys. Status Solidi (a) **9**, 679–689 (1972).

[44] T. Kimura, G. Lawes, and A. P. Ramirez, Phys. Rev. Lett. **94**, 137201 (2005).

[45] Y. S. Chai, S. H. Chun, J. Z. Cong, and K. H. Kim, Phys. Rev. B **98**, 104416 (2018).

[46] T. Tsutaoka, J. Appl. Phys. **93**, 2789–2796 (2003).

[47] S. Kim, S. Jang, S. Byun, J. Lee, J. Joo, S. Jeong, and M.-J. Park, J. Appl. Polym. Sci. **87**, 1969–1974 (2003).

[48] R. C. Pullar, Prog. Mater. Sci. **57**, 1191–1334 (2012).

[49] H. Kojima, Handbook of Ferromagnetic Materials **3**, 305–391 (1982).

[50] J. Hankiewicz, Z. Pajak, and A. Murakhowski, J. Magn. Magn. Mater. **101**, 134–136 (1991).

[51] H. Štěpánková, J. Englich, J. Kohout, and H. Lütgemeier, J. Magn. Magn. Mater. **140–144**, 2099–2100 (1995).

[52] G. Albanese, E. Calabrese, A. Deriu, and F. Licci, Hyperfine Interact. **28**, 487–489 (1986).

[53] X. Z. Zhou, I. Horio, A. H. Morrish, Z. W. Li, and K. Hanawa, IEEE Trans. Magn. **27**, 4651–4653 (1991).

[54] R. L. Streever, Phys. Rev. **186**, 285–290 (1969).

[55] R. F. W. Bader, *Atoms in molecules – a quantum theory* (University of Oxford Press, Oxford, 1990).

[56] H. Štěpánková, J. Englich, J. Kohout, and H. Lütgemeier, J. Magn. Magn. Mater. **140–144**, 2099–2100 (1995).

[57] F. K. Lotgering, J. Phys. Chem. Solids **35**, 1663–1669 (1974).

[58] R. Grössinger, M. Küpferling, M. Haas, H. Müller, G. Wiesinger, and C. Ritter, J. Magn. Magn. Mater **310**, 2587–2589 (2007).

[59] H. Štěpánková, J. Englich, P. Novák, and H. Lütgemeier, J. Magn. Magn. Mater **104–107**, 409–410 (1992).

[60] A. I. Liechtenstein, V. I. Anisimov, and J. Zaanen, Phys. Rev. B **52**, R5467–R5470 (1995).

[61] S. L. Dudarev, G. A. Botton, S. Y. Savrasov, C. J. Humphreys, and A. P. Sutton, Phys. Rev. B **57**, 1505–1509 (1998).

[62] P. Novák, K. Knížek, M. Küpferling, R. Grössinger, and M. W. Pieper, Eur. Phys. J. B **43**, 509–515 (2005).

[63] W. Zhang, K. Koepernik, M. Richter, and H. Eschrig, Phys. Rev. B **79**, 155123 (2009).

[64] B. Dorado, B. Amadon, M. Freyss, and M. Bertolus, Phys. Rev. B **79**, 235125 (2009).

[65] G. Jomard, B. Amadon, F. Bottin, and M. Torrent, Phys. Rev. B **78**, 075125 (2008).

[66] S. Abdelouahed and M. Alouani, Phys. Rev. B **79**, 054406 (2009).

[67] B. T. Shirk and W. R. Buessem, J. Appl. Phys. **40**, 1294–1296 (1969).

[68] J. Buršík, I. Drbohlav, Z. Frait, K. Knížek, R. Kužel, and K. Kouřil, J. Solid State Chem. **184**, 3085–3094 (2011).

[69] P. Novák, K. Knížek, and J. Rusz, Phys. Rev. B **76**, 024432 (2007).

[70] K. Knížek, P. Novák, and M. Küpferling, Phys. Rev. B **73**, 153103 (2006).

[71] F. Walz, J. Phys. Condens. Matter **14**, R285–R340 (2002).

[72] Y. Joly, J. E. Lorenzo, E. Nazarenko, J.-L. Hodeau, D. Mannix, and C. Marin, Phys. Rev. B **78**, 134110 (2008).

[73] Z. Kakol and J. M. Honig, Phys. Rev. B **40**, 9090–9097 (1989).

[74] Z. Kakol, J. Sabol, J. Stickler, and J. M. Honig, Phys. Rev. B **46**, 1975–1978 (1992).

[75] I. Biało, A. Kozłowski, M. Wack, A. Włodek, Ł. Gondek, Z. Kakol, R. Hochleitner, A. Zywczak, V. Chlan, and S. A. Gilder, Geophys. J. Int. **219**, 148–158 (2019).

[76] L. Carporzen and S. A. Gilder, J. Geophys. Res. **115** (2010).

[77] M. Senn, J. Wright, and J. Attfield, Nature **481**, 173–176 (2012).

[78] P. Novák, H. Štěpánková, J. Englich, and J. Kohout, Phys. Rev. B **61**, 1256–1260 (2000).

[79] M. Mizoguchi, J. Phys. Soc. Jpn. **70**, 2333–2344 (2001).

[80] K. Abe, Y. Miyamoto, and S. Chikazumi, J. Phys. Soc. Jpn. **41**, 1894–1902 (1976).

[81] C. Patterson, Phys. Rev. B **90** (2014).

[82] B. A. Calhoun, Phys. Rev. **94**, 1577–1585 (1954).

[83] V. Chlan, K. Kouřil, H. Štěpánková, J. Řezníček R. and Štěpánek, W. Tabis, G. Krol, Z. Tarnawski, and A. Kakol Z. and Kozłowski, J. Appl. Phys. **108**, 083914 (2010).

[84] J. E. Lorenzo, C. Mazzoli, N. Jaouen, C. Detlefs, D. Mannix, S. Grenier, Y. Joly, and C. Marin, Phys. Rev. Lett. **101**, 226401 (2008).

[85] A. Bosak, D. Chernyshov, M. Hoesch, P. Piekarz, M. Le Tacon, M. Krisch, A. Kozłowski, A. M. Oleś, and K. Parlinski, Phys. Rev. X **4**, 011040 (2014).

[86] V. Chlan, J. Zukrowski, A. Bosak, Z. Kakol, Z. Kozłowski A. and Tarnawski, R. Řezníček, H. Štěpánková, I. Novák P. and Bialo, and J. M. Honig, Phys. Rev. B **98**, 125138 (2018).

[87] J. C. Slonczewski, Phys. Rev. **110**, 1341–1348 (1958).

[88] R. Aragón, Phys. Rev. B **46**, 5334–5338 (1992).

[89] V. Skumryev, H. J. Blythe, J. Cullen, and J. M. D. Coey, J. Magn. Magn. Mater. **196–197**, 515–517 (1999).

[90] D. Torumba, K. Parlinski, M. Rots, and S. Cottenier, Phys. Rev. B **74**, 144304 (2006).

[91] R. Laskowski, G. K. H. Madsen, P. Blaha, and K. Schwarz, Phys. Rev. B **69**, 140408 (2004).

[92] D. Padro, V. Jennings, M. E. Smith, R. Hoppe, P. A. Thomas, and R. Dupree, J. Phys. Chem. B **106**, 13176–13185 (2002).

[93] L. Bosio, J. Chem. Phys. **68**, 1221–1223 (1978).

[94] O. Degtyareva, M. I. McMahon, D. R. Allan, and R. J. Nelmes, Phys. Rev. Lett. **93**, 205502 (2004).

[95] T. Kenichi, K. Kazuaki, and A. Masao, Phys. Rev. B **58**, 2482–2486 (1998).

[96] G. B. Parravicini, A. Stella, P. Ghigna, G. Spinolo, A. Migliori, F. d'Acapito, and R. Kofman, Appl. Phys. Lett. **89**, 033123 (2006).

[97] D. Hechtfischer, R. Karcher, and K. Luders, J. Phys. F **3**, 2021–2022 (1973).

[98] N. C. Halder, J. Magn. Reson. **15**, 339–343 (1974).

[99] M. Huebner, T. Wagner, S. Götz, and G. Eska, Physica B **210**, 484–495 (1995).

[100] M. I. Valic and D. L. Williams, J. Phys. Chem. Solids **33**, 1583–1602 (1972).

[101] J. D. Stroud and S. L. Segel, J. Phys. F **5**, 1981–1985 (1975).

[102] T. Meier, Annu. Rep. NMR Spectrosc. **93**, 1–74 (2018).

[103] F. Birch, Phys. Rev. **71**, 809–824 (1947).

[104] D. T. Adroja, A. del Moral, C. de la Fuente, A. Fraile, E. A. Goremychkin, J. W. Taylor, A. D. Hillier, and F. Fernandez-Alonso, Phys. Rev. Lett. **108**, 216402 (2012).

[105] D. M. Nisson, A. P. Dioguardi, P. Klavinsand, C. H. Lin, K. Shirer, A. C. Shockley, J. Crocker, and N. J. Curro, Phys. Rev. B **87**, 195202 (2013).

[106] S. Mukhopadhyay, S. Krämer, H. Mayaffre, H. F. Legg, M. Orlita, C. Berthier, M. Horvatić, G. Martinez, M. Potemski, B. A. Piot, A. Materna, G. Strzelecka, and A. Hruban, Phys. Rev. B **91**, 081105 (2015).

[107] H. Ogino, A. Yoshikawa, M. Nikl, J. A. Mares, J. Shimoyama, and K. Kishio, J. of Cryst. Growth **311**, 908–911 (2009).

Commented papers

[VC1] P. Novák and V. Chlan, "Contact hyperfine field at Fe nuclei from density functional calculations", Phys. Rev. B **81**, 174412 (2010) 10.1103/PhysRevB.81.174412.

[VC2] V. Chlan, H. Štěpánková, R. Řezníček, and P. Novák, "Anisotropy of hyperfine interactions as a tool for interpretation of NMR spectra in magnetic materials", Solid State Nucl. Magn. Reson. **40**, 27–30 (2011) 10.1016/j.ssnmr.2011.04.002.

[VC3] J. Toepfer, D. Seifert, J.-M. Le Breton, F. Langenhorst, V. Chlan, K. Kouřil, and H. Štěpánková, "Hexagonal ferrites of X-, W-, and M-type in the system Sr-Fe-O: A comparative study", J. Solid State Chem. **226**, 133–141 (2015) 10.1016/j.jssc.2015.02.007.

[VC4] V. Chlan, K. Kouřil, K. Uličná, H. Štěpánková, J. Toepfer, and D. Seifert, "Charge localization and magnetocrystalline anisotropy in La, Pr, and Nd substituted Sr hexaferrites", Phys. Rev. B **92**, 125125 (2015) 10.1103/PhysRevB.92.125125.

[VC5] V. Chlan, K. Kouřil, and H. Štěpánková, "Hyperfine fields and lattice deformations in Ba and Sr hexaferrites", Acta Phys. Pol. A **127**, 594–596 (2015) 10.12693/APhysPolA.127.594.

[VC6] K. Kouřil, V. Chlan, H. Štěpánková, P. Novák, K. Knížek, J. Hybler, T. Kimura, Y. Hiraoka, and J. Bursik, "Hyperfine interactions in magnetoelectric hexaferrite system", J. Magn. Magn. Mater. **322**, 1243–1245 (2010) 10.1016/j.jmmm.2009.03.011.

[VC7] K. Kouřil, V. Chlan, H. Štěpánková, A. Telfah, P. Novák, K. Knížek, Y. Hiraoka, and T. Kimura, "Distribution of Zn in magnetoelectric Y-Type hexaferrite", Acta Phys. Pol. A **118**, 732–733 (2010) 10.12693/APhysPolA.118.732.

[VC8] V. Chlan, K. Kouřil, H. Štěpánková, R. Řezníček, and J. Englich, "Study of Y-type hexaferrite by means of Fe-57 NMR and electronic structure calculations", Acta Phys. Pol. A **126**, 42–43 (2014) 10.12693/APhysPolA.126.42.

[VC9] R. Řezníček, V. Chlan, H. Štěpánková, and P. Novák, "Hyperfine field and electronic structure of magnetite below the Verwey transition", Phys. Rev. B **91**, 125134 (2015) 10.1103/PhysRevB.91.125134.

[VC10] R. Řezníček, V. Chlan, H. Štěpánková, P. Novák, J. Zukrowski, A. Kozłowski, Z. Kakol, Z. Tarnawski, and J. M. Honig, "Understanding the Mössbauer spectrum of magnetite below the Verwey transition: Ab initio calculations, simulation, and experiment", Phys. Rev. B **96**, 195124 (2017) 10.1103/PhysRevB.96.195124.

[VC11] R. Řezníček, V. Chlan, H. Štěpánková, P. Novák, and M. Maryško, "Magnetocrystalline anisotropy of magnetite", J. Phys. Condens. Matter **24**, 055501 (2012) 10.1088/0953-8984/24/5/055501.

[VC12] V. Chlan, P. Novák, H. Štěpánková, J. Englich, J. Kuriplach, and D. Nižňanský, "Hyperfine interactions in lutetium iron garnet", J. Appl. Phys. **99**, 08M903 (2006) 10.1063/1.2158687.

[VC13] V. Procházka, H. Štěpánková, V. Chlan, J. Tuček, J. Čuda, K. Kouřil, J. Filip, and R. Zbořil, "Electric field gradient in $FeTiO_3$ by nuclear magnetic resonance and ab initio calculations", J. Phys. Condens. Matter **23**, 205503 (2011) 10.1088/0953-8984/23/20/205503.

[VC14] R. Řezníček, V. Chlan, and J. Haase, "NMR and ab initio study of gallium metal under pressure", Phys. Rev. B **99**, 125121 (2019) 10.1103/PhysRevB.99.125121.

[VC15] V. Chlan, P. Doležal, R. Sgallová, M. Klicpera, C. Franz, and P. Javorský, "Local atomic arrangement in $LaCuAl_3$ and $LaAuAl_3$ by NMR and density functional theory", J. Phys. Condens. Matter **31**, 385601 (2019) 10.1088/1361-648X/ab27ac.

[VC16] R. Gühne, V. Chlan, G. V. M. Williams, V. S. Chong, K. Kadowaki, A. Poeppl, and J. Haase, "Unusual Bi-209 NMR quadrupole effects in topological insulator Bi_2Se_3", J. Magn. Reson. **302**, 34–42 (2019) 10.1016/j.jmr.2019.03.008.

[VC17] Y. O. Zagorodniy, V. Chlan, H. Štěpánková, Y. Fomichov, J. Pejchal, V. V. Laguta, and M. Nikl, "Gallium preference for the occupation of tetrahedral sites in $Lu_3(Al_{5-x}Ga_x)O_{12}$ multicomponent garnet scintillators according to solid-state nuclear magnetic resonance and density functional theory calculations", J. Phys. Chem. Solids **126**, 93–104 (2019) 10.1016/j.jpcs.2018.10.027.